Supporting Information

Solvation Engineering Decouples Bulk and Interfacial Chemistry for Robust Potassium-Ion Batteries

Dianwei Zhang[1, 2, #], Hongwei Fu[1, 2, #], Xuemei Ma[1, 2, #], Apparao M. Rao[3], Yihan Yang[1, 2], Fuxiang Li[1, 2], Xiazhen Li[4], Jiang Zhou[5], and Bingan Lu[1, 2, 6, *].

[1]School of Physics and Electronics, Hunan University, Changsha 410082, P. R. China.

[2]Yuelushan Center for Industrial innovation, Hunan University, Changsha 410082, P. R. China.

[3]Department of Physics and Astronomy, Clemson Nanomaterials Institute, Clemson University, Clemson, SC 29634, USA.

[4]School of Materials and Energy, Central South University of Forestry and School of Materials and Energy, Central South University of Forestry and Technology, Changsha 410004, P. R. China.

[5]School of Materials Science and Engineering, Central South University, Changsha 410083, P. R. China.

[6]State Key Laboratory of New Textile Materials and Advanced Processing, Wuhan Textile University, Wuhan 430200, China.

[#]These authors contributed equally

*Corresponding author: Email: luba2012@hnu.edu.cn (B. L.).

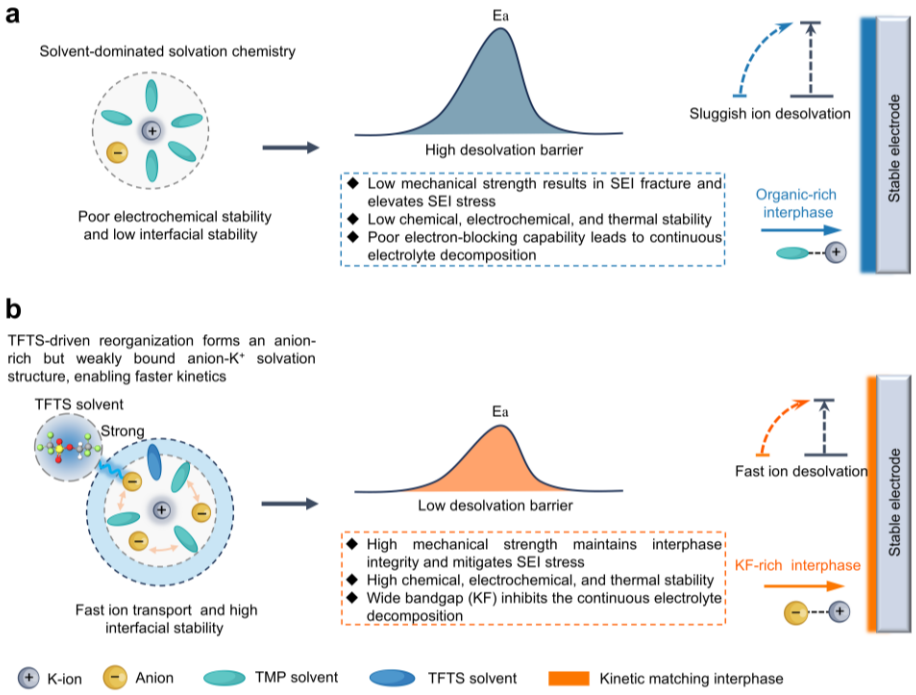

Supplementary Fig. 1. **a**, The 1 M TMP electrolyte without TFTS addition exhibits a solvent-dominated solvation structure, resulting in poor electrochemical stability, low interfacial stability, and low K^+ transport kinetics. **b**, The TFTS-based electrolyte features a distinctive anion-rich solvation structure with fewer solvent ligands, enabling high interfacial stability and fast K-ion transport kinetics. The key characteristics of the interphase derived from these electrolytes are described in the rectangles of corresponding colors.

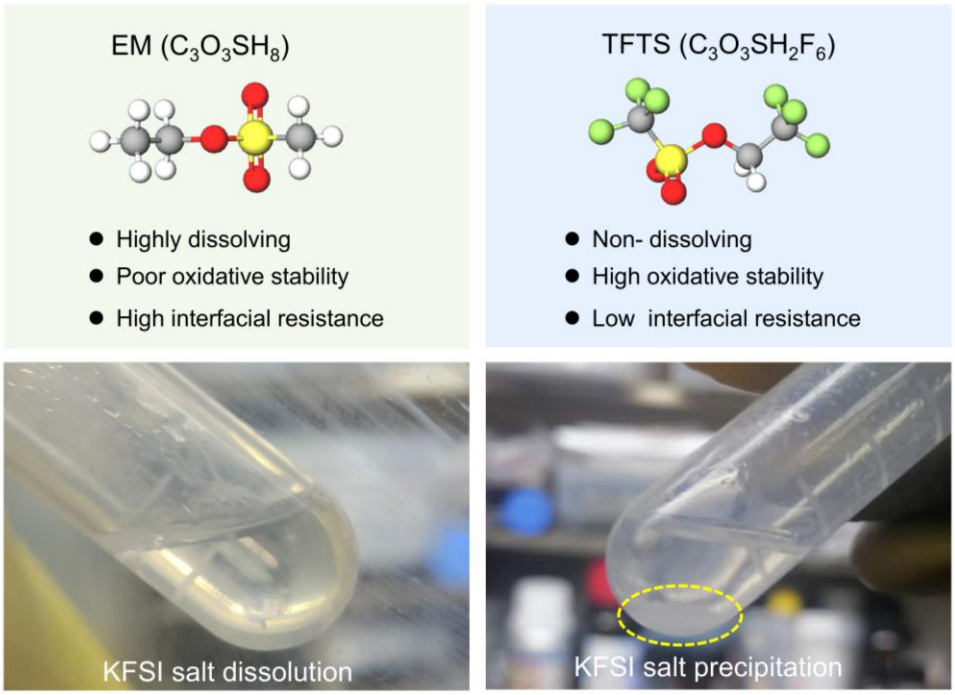

Supplementary Fig. 2. Digital photograph of KFSI salt dissolved in EM (ethyl methanesulfonate) and TFTS solvent, respectively. Atomic color code: yellow, S; red, O; green, F; Gray, C; white, H.

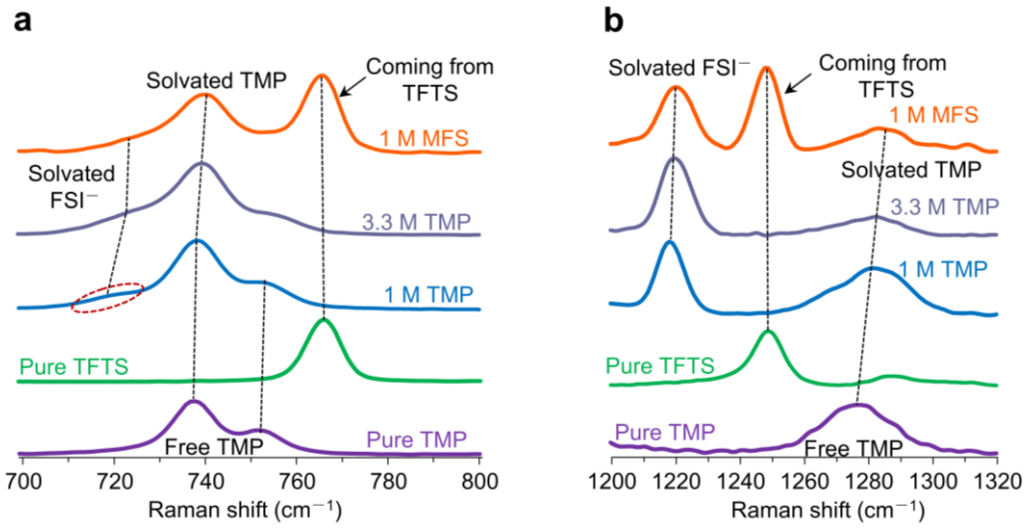

Supplementary Fig. 3. **a**, Raman spectra in the 700-800 cm^{-1} region. **b**, Raman spectra in the 1200-1320 cm^{-1} region. Spectra are shown for TMP solvent, TFTS solvent, 1 M TMP electrolyte, 1 M MFS electrolyte, and 3.3 M TMP electrolyte.

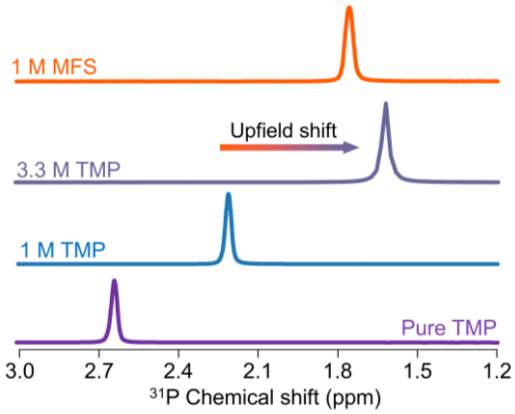

Supplementary Fig. 4. ^{31}P NMR spectrum of TMP solvent and the investigated electrolytes (1 M TMP electrolyte, 3.3 M TMP electrolyte, and 1 M MFS electrolyte).

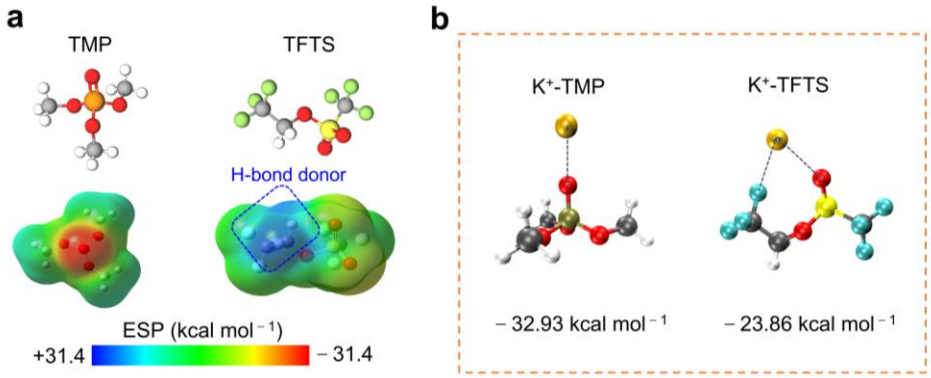

Supplementary Fig. 5. **a**, Electrostatic potential map of TMP and TFTS. **b**, Binding energies of TMP-K^+ and TFTS-K^+. Atomic color code: brown, P; yellow, S; red, O; light blue, F; Gray, C; white, H; golden, K^+.

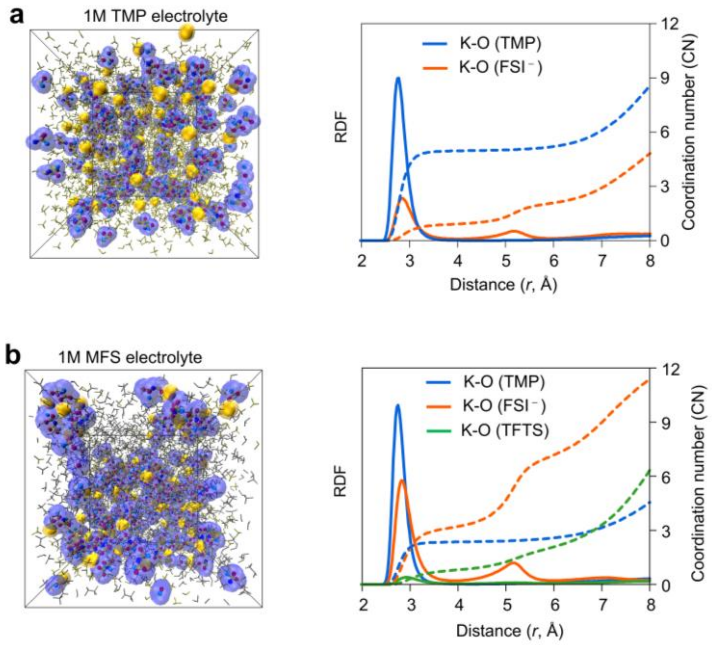

Supplementary Fig. 6. **a**, **b**, Molecular dynamics (MD) simulation snapshots, radial distribution function (RDF, solid lines), and coordination number (CN, dashed lines) for (**a**) 1 M TMP electrolyte and (**b**) 1 M MFS electrolyte. In MD simulation snapshots, the blue isosurfaces highlight the locations of FSI^- anions; the golden ball represents K^+.

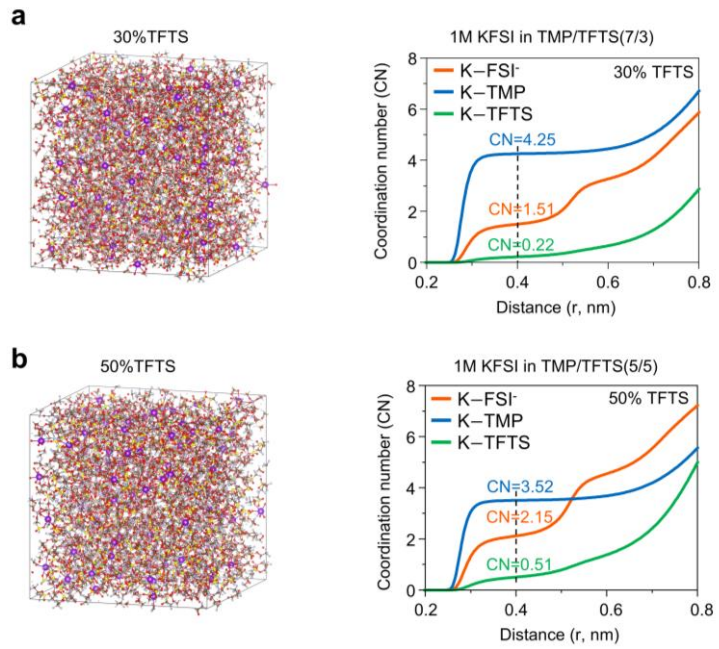

Supplementary Fig. 7. **a**, **b**, MD snapshot and coordination number for the TFTS-based electrolyte with volume ratio of (**a**) 30%TFTS and (**b**) 50% TFTS.

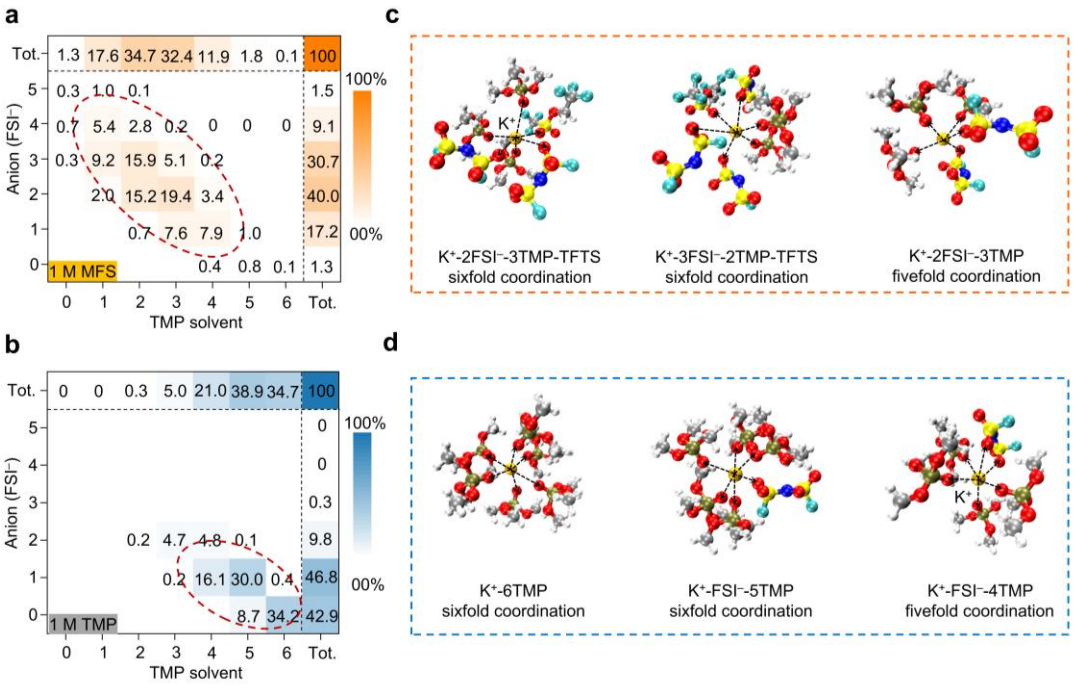

Supplementary Fig. 8. **a**, **b**, Probability densities of specific solvation structure stoichiometry in 1 M MFS electrolyte (**a**) and 1 M TMP electrolyte (**b**) at 298 K. **c**, **d**, Representative K^+ solvation clusters with sixfold coordination and fivefold coordination in 1 M MFS electrolyte (**c**) and 1 M TMP electrolyte (**d**). Atomic color code: brown, P; yellow, S; red, O; light blue, F; Gray, C; white, H; deep blue, N; golden, K^+.

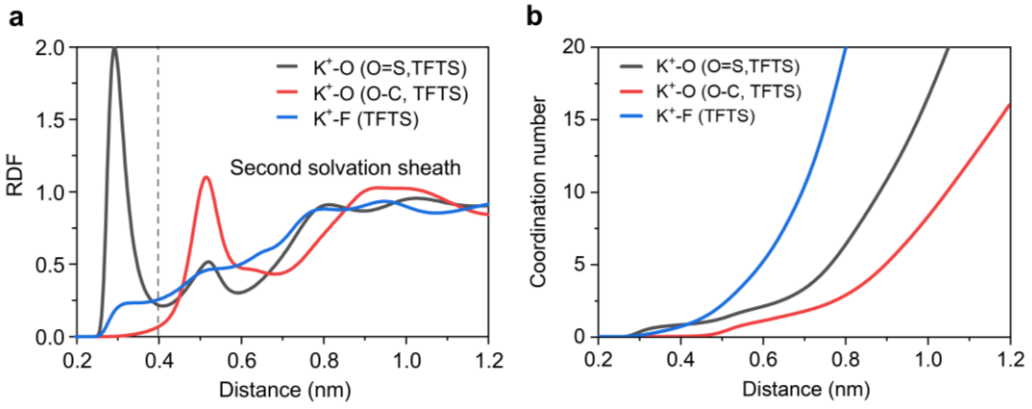

Supplementary Fig. 9. **a**, RDF for K^+-O (TFTS) and K^+-F (TFTS) in 1 M MFS electrolyte at 298 K. **b**, CN for K^+-O (TFTS) and K^+-F (TFTS) in 1 M MFS electrolyte at 298 K

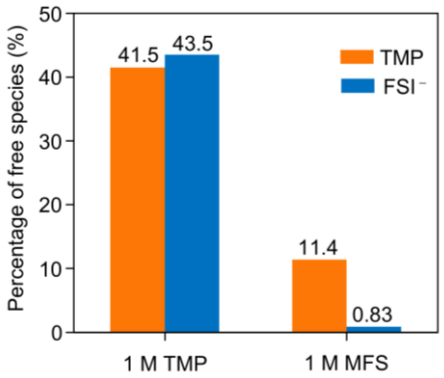

Supplementary Fig. 10. Percentage of free TMP and free FSI^- species in 1 M TMP electrolyte and 1 M MFS electrolyte.

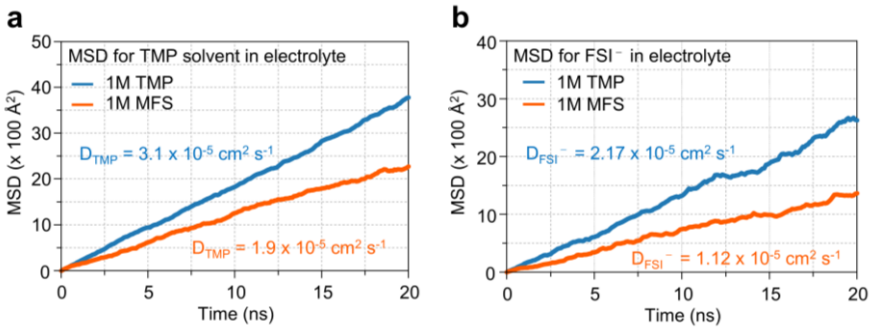

Supplementary Fig. 11. **a**, **b**, Mean squared displacements (MSD) of TMP molecules (**a**) and FSI^- anions (**b**) in 1 M TMP electrolyte and 1 M MFS electrolyte.

To further evaluate the TMP molecules and FSI^- anions mobility, MD simulation was conducted to calculate the mean squared displacement (MSD) of TMP and FSI^-, using the following equation:

$$\text{MSD}\ (t) = \ |r(t) - r(t_0)|^2 \qquad (1)$$

The MSD analysis provides insights into the diffusion behavior of TMP and FSI^- within 20 ns. A steeper slope of the MSD plot indicates a higher diffusion coefficient (D), which reflects a greater TMP and FSI^- mobility. The diffusion coefficient value can be determined from the MSD using the following relationship:

$$D = \frac{1}{6N} \lim_{t\to\infty} \frac{d}{dt} \sum_{i=1}^{n} \{|r(t) - r(t_0)|^2\} \qquad (2)$$

The diffusion coefficient for each electrolyte can be estimated, by calculating the slope of the MSD plot, enabling a comparison of the diffusion kinetics.

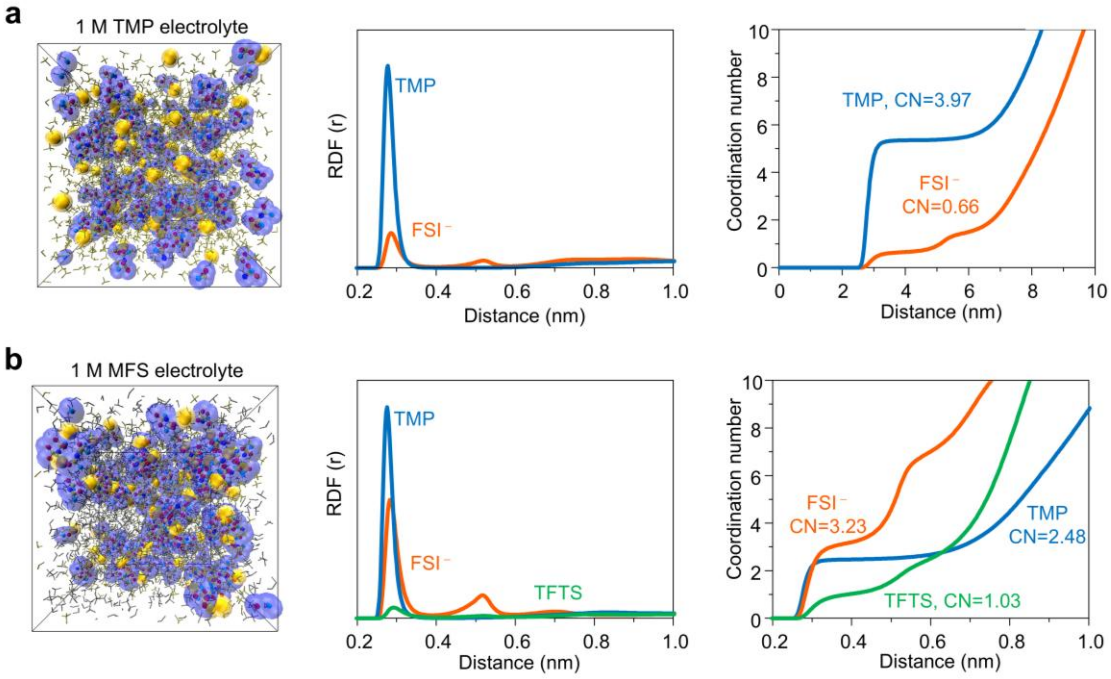

Supplementary Fig. 12. **a**, **b**, MD snapshot, RDF, and CN for the 1 M TMP electrolyte (**a**) and 1 M MFS electrolyte (**b**) at 253 K. In MD simulation snapshots, the blue isosurfaces highlight the locations of FSI^- anions; the golden ball represents K^+.

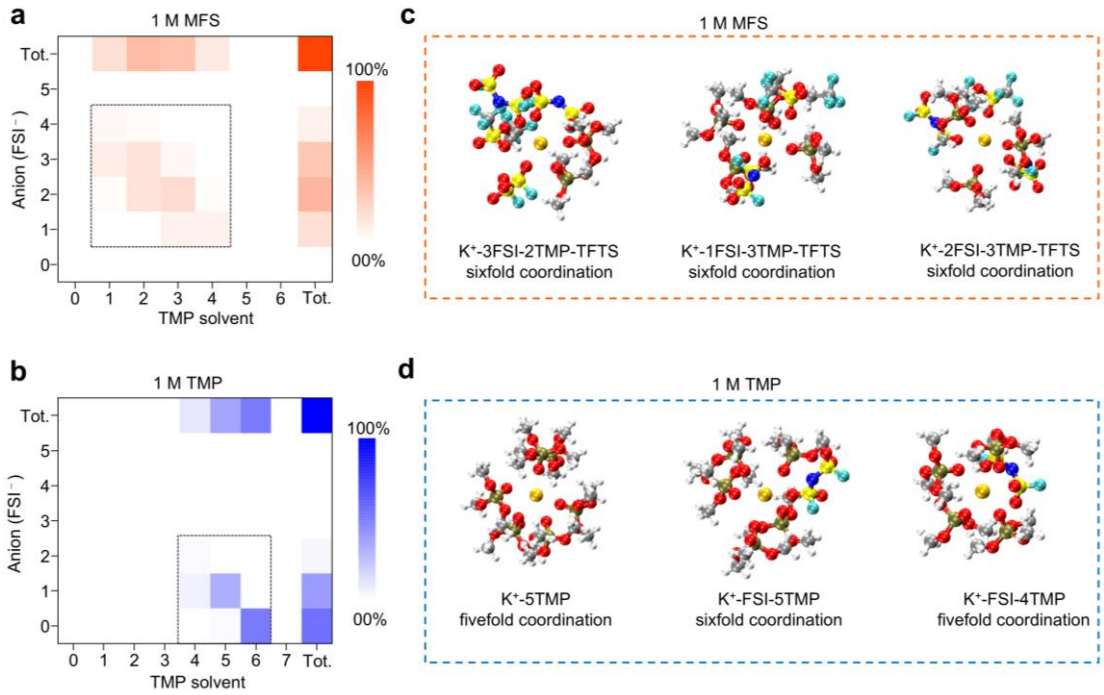

Supplementary Fig. 13 | Solvation structure analysis at 253 K. **a**, **b**, Specific solvation structure stoichiometry probability densities in 1 M MFS electrolyte (**a**) and 1 M TMP electrolyte (**b**). **c**, Representative K^+ solvation clusters with sixfold coordination in 1 M MFS electrolyte. **d**, Representative K^+ solvation clusters with sixfold and fivefold coordination in 1 M TMP electrolyte. Atomic color code: brown, P; yellow, S; red, O; light blue, F; Gray, C; white, H; deep blue, N; golden, K^+.

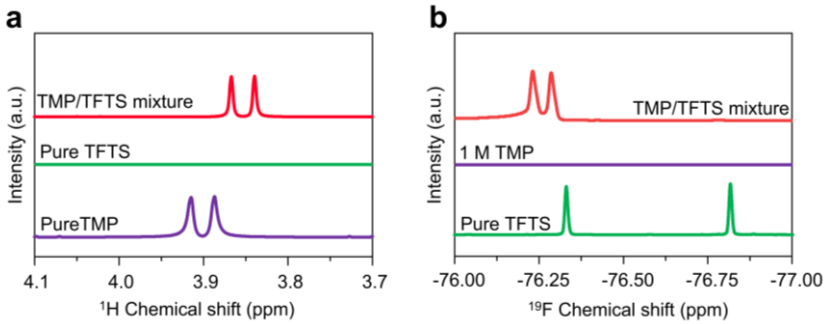

Supplementary Fig. 14. **a**, ^{1}H NMR spectra of pure TMP and the TMP-TFTS mixture. **b**, ^{19}F NMR spectra of pure TFTS solvent and the TMP-TFTS mixture.

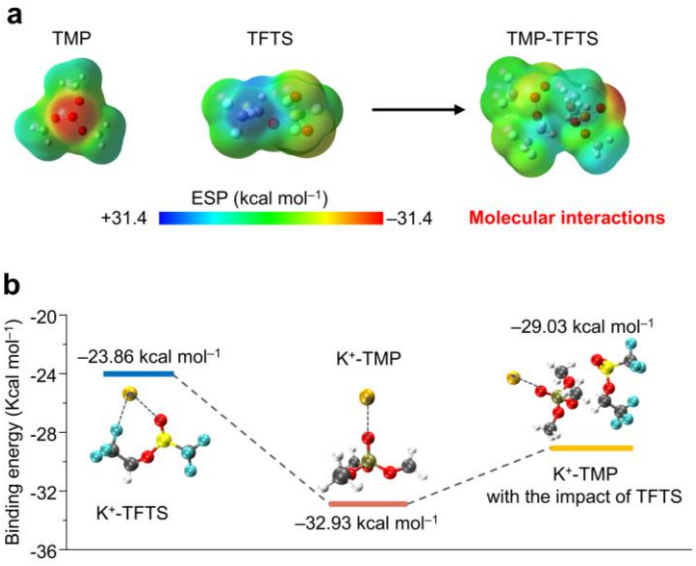

Supplementary Fig. 15. **a**, Electrostatic potential calculation of TMP-TFTS interaction. **b**, Optimized complex configurations and corresponding binding energies of solvent and K^+. Atomic color code: brown, P; yellow, S; red, O; light blue, F; Gray, C; white, H; golden, K^+.

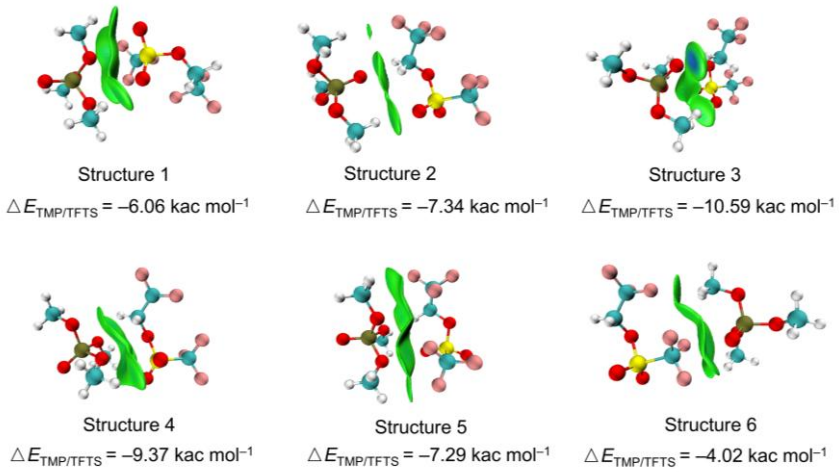

Supplementary Fig. 16. Gradient isosurfaces and interaction energies of TMP and TFTS. The surface is shown on a blue-green-red scale from -0.04 to 0.02 arb. units. Atomic color code: brown, P; yellow, S; red, O; pink, F; light blue, C; white, H.

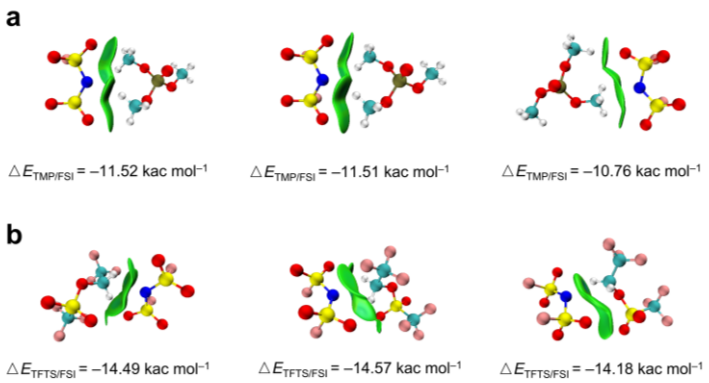

Supplementary Fig. 17. **a**, **b**, Gradient isosurfaces and interaction energies of TMP-FSI^- (**a**) and TFTS-FSI^- (**b**). The surface is shown on a blue-green-red scale from -0.04 to 0.02 arb. units. Atomic color code: brown, P; yellow, S; red, O; pink, F; light blue, C; white, H.

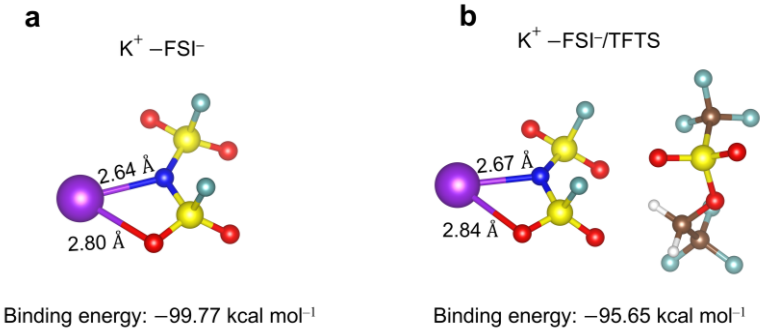

Supplementary Fig. 18. **a**, Optimized complex configurations and corresponding binding energy of FSI^--K^+ in the absence of TFTS. **b**, Optimized complex configurations and corresponding binding energy of FSI^--K^+ in the presence of TFTS. Atomic color code: yellow, S; red, O; light blue, F; brown, C; white, H; purple, K^+. All structures were visualized using VESTA Software

.

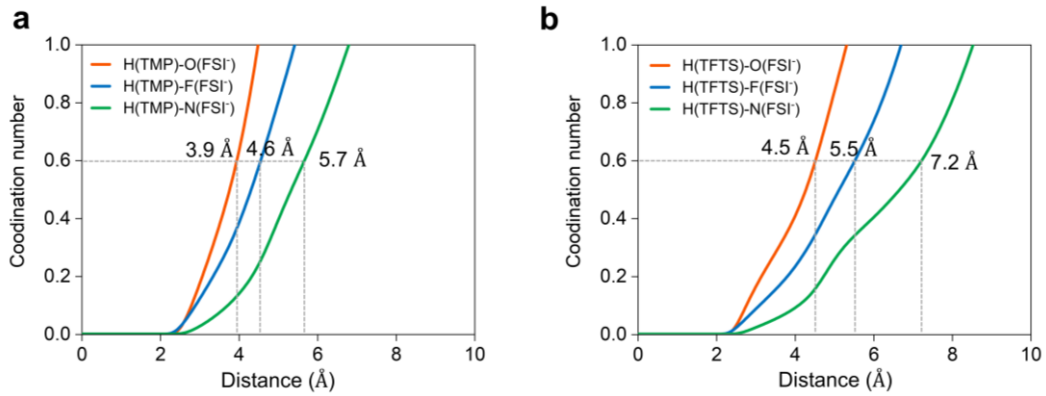

Supplementary Fig. 19. **a**, CN of TMP-FSI^- in 1 M MFS electrolyte. **b**, CN of TFTS-FSI^- in 1 M MFS electrolyte.

As shown in Supplementary Fig. 19, under the same coordination number between solvent and FSI^-, TMP is located at a shorter distance, whereas TFTS is located at a longer distance. These results confirm that TMP mainly forms strong anion-dipole interactions with FSI^- anions inside the K^+ primary solvation sheath, while TFTS, mainly distributed outside the K^+ primary solvation stealth, primarily exerts an outer-guiding effect on solvated FSI^- anions by strong hydrogen bond.

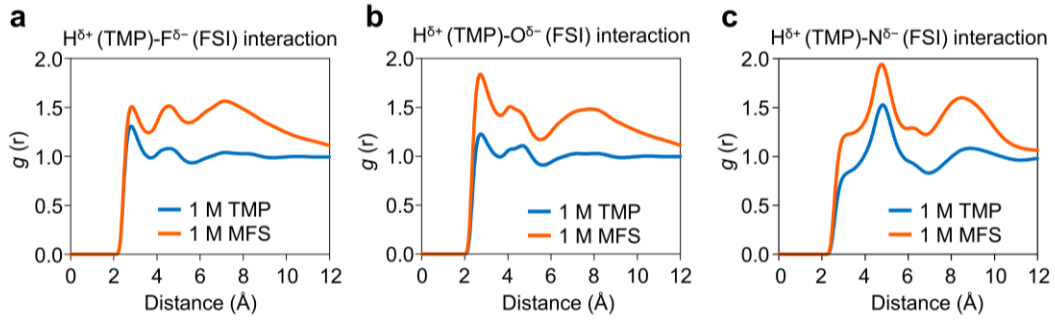

Supplementary Fig. 20. **a-c**, Comparison of RDF for (**a**) $H_{(TMP)}$ -$F_{(FSI^-)}$, (**b**) $H_{(TMP)}$-$O_{(FSI^-)}$, and (**c**) $H_{(TMP)}$-$N_{(FSI^-)}$ pairs in the 1 M TMP electrolyte and the1 M MFS electrolyte. Generally speaking, the greater the RDF peak value, the higher probability of atom appearance.

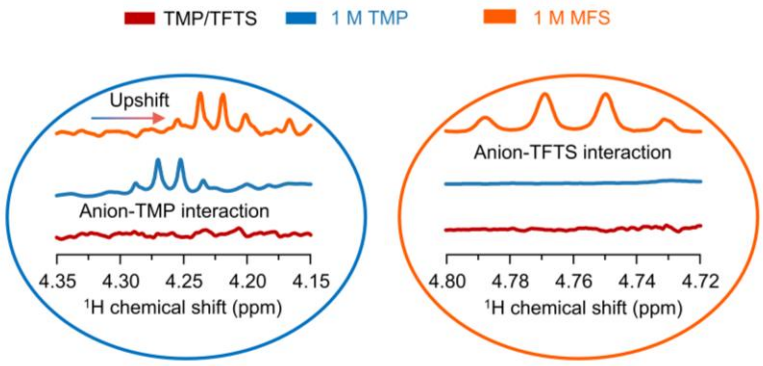

Supplementary Fig. 21. Amplified ^{1}H NMR spectra of the TMP/TFTS mixture, 1 M TMP electrolyte, and 1 M MFS electrolyte in the range of 4.30-4.20 ppm and 4.80-4.72 ppm.

As shown in Supplementary Fig. 21, new ^{1}H-NMR peaks around 4.30-4.20 ppm and 4.80-4.72 ppm emerged in both 1 M KFSI TMP and 1 M KFSI TMP/TFTS electrolytes upon the addition of KFSI salt that can be identified as the TMP−FSI^- anion and TFTS−FSI^- anion pairs interaction, which is again absent in the mixed solution of TMP/TFTS without KFSI salt addition[1, 2]. On the one hand, the replacement of TFTS weakens the overall solvation ability of the electrolyte, facilitating the competitive coordination between TMP solvents and FSI^- anions for K^+. This leads to the high-frequency contact between TMP and FSI^- anions within the K^+ primary solvation sheath (in agreement with the RDF data in Supplementary Fig. 20) and simultaneously induces the enhanced TMP−FSI^- interaction. Therefore, after the introduction of TFTS solvent, an upfield shifted ^{1}H-NMR signals is observed in the 1 M MFS electrolyte around 4.30-4.20 ppm compared to the 1 M TMP electrolyte. On the other hand, due to the strong TFTS−FSI^- interactions through hydrogen bond, TFTS located outside the PSS exerts an outer-guiding effect on the solvated FSI^- anions. Such enhanced anion-dipole interactions of TMP−FSI^- that is induced by TFTS and the outer-guiding effect on the solvated FSI^- anions by TFTS addition, can thermodynamically weaken the strong coulombic interaction between K^+ and FSI^-anion within the primary solvation shell.

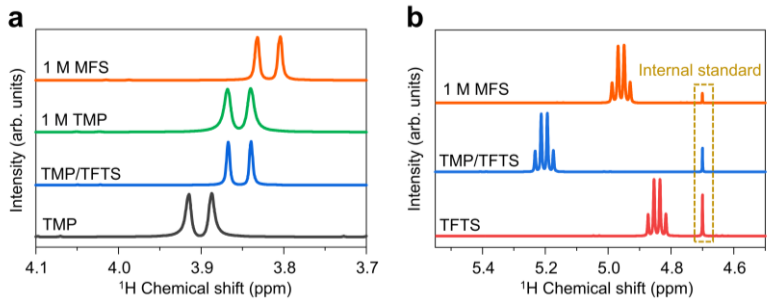

Supplementary Fig. 22. **a**, ^{1}H NMR spectra of TMP, TMP/TFTS, 1 M TMP, and 1 M MFS solutions. **b**, ^{1}H NMR spectra of TFTS, TMP/TFTS, and 1 M MFS solutions.

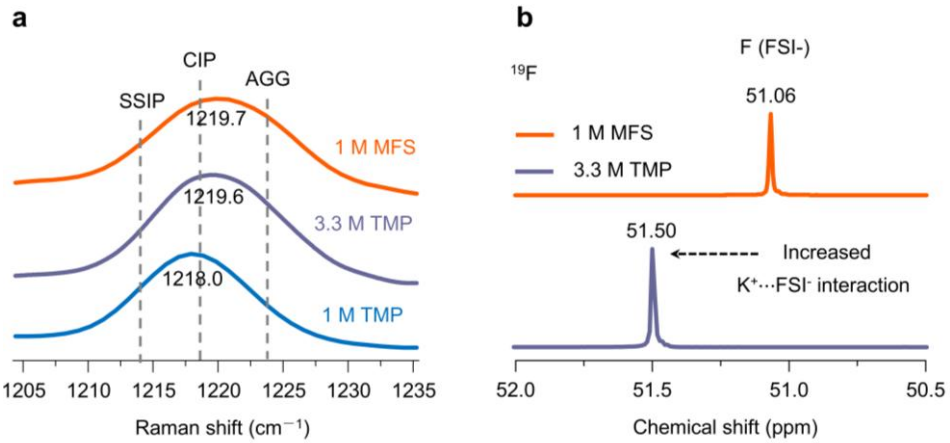

Supplementary Fig. 23. **a**, Distribution of solvated species in three electrolytes from Raman spectra (without deconvolution): solvent-separated-ion-pairs (SSIP; 1213 cm^{-1}), contact-ion-pairs (CIP; 1218 cm^{-1}), and cation-anion aggregates (AGG; 1223 cm^{-1}). **b**, ^{19}F NMR spectra of 3.3 M TMP electrolyte and 1 M MFS electrolyte.

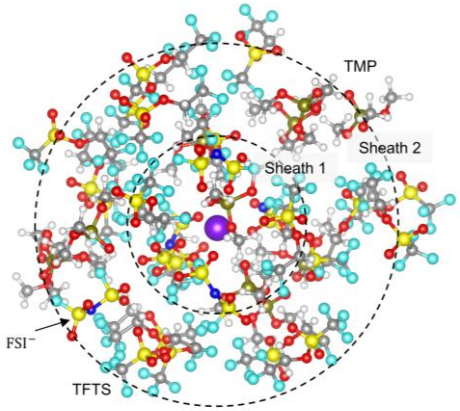

Supplementary Fig. 24. Locally enlarged 3D snapshot of K^+ solvation structure in 1 M MFS electrolyte from MD simulation. The final construction was visualized with VESTA. Atomic color code: brown, P; yellow, S; red, O; light blue, F; gray, C; white, H; purple, K^+.

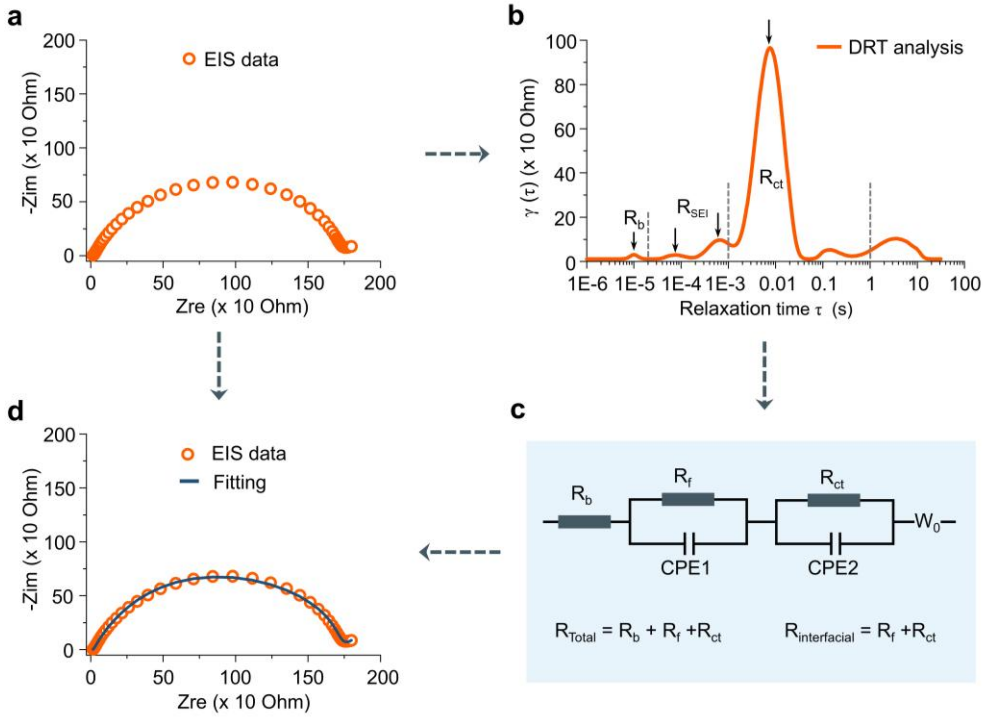

Supplementary Fig. 25. **a**, **b**, Experimental Nyquist plot (**a**) of a K-symmetric cell in 1 M MFS electrolyte at 298 K and corresponding DRT analysis (**b**). **c**, Equivalent circuit model used for fitting. **d**, Fitted Nyquist plot (solid line) superimposed on the experimental EIS data (hollow circle).

The EIS data of the K-symmetric cells were fitted using an equivalent circuit model of R_b -(R_fCPE1)-($R_{ct}CPE2$)- W_0 (Supplementary Fig. 25c), where R_0, R_f, and R_{ct} represent the bulk resistance, film resistance (mainly dominated by K^+ through the SEI film), and charge-transfer resistance (mainly dominated by K^+ desolvation), respectively. The total of R_f and R_{ct} is considered as the interfacial resistance ($R_{interfacial}$). CPE (constant phase element) was used to account for the non-ideal capacitive behavior. This equivalent circuit has also been applied to fit the EIS data of Li or Na-symmetric cells[3, 4]. To further verify the reasonability of this circuit, DRT analysis was conducted. As shown in Supplementary Fig. 25b, the DRT profiles exhibit distinct peaks at characteristic relaxation times (τ, s), which can be assigned to the processes of K^+ crossing the SEI film and charge transfer processes, respectively. These results are consistent with the selected equivalent circuit model, confirming the validity of the fitting model for the K-symmetric cells.

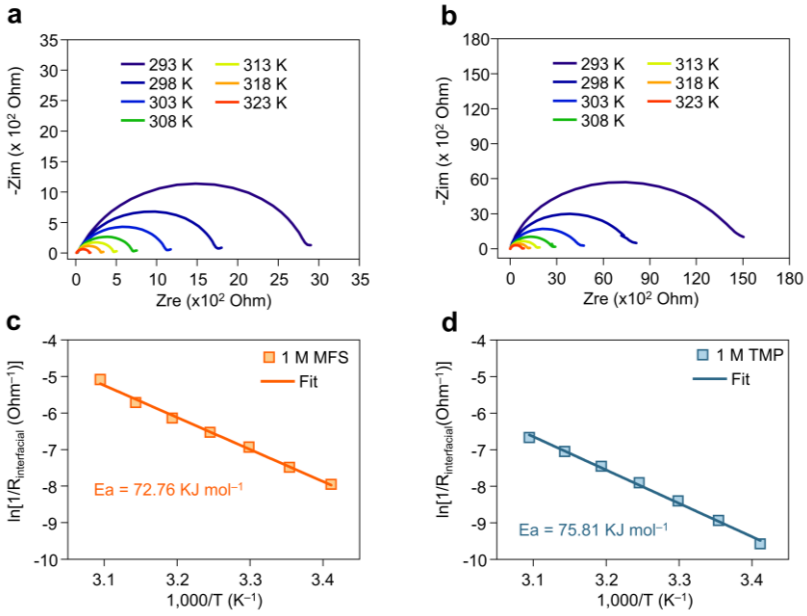

Supplementary Fig. 26. **a**, **b**, Resistance measurements of symmetrical K||K cells as a function of temperature (293-323 K) in 1 M MFS (**a**) and 1 M TMP (**b**) electrolytes. **c**, **d**, Corresponding Arrhenius plots used to determine the activation energy (E_a) for interfacial transport in 1 M MFS electrolyte (**c**) and 1 M TMP electrolyte (**d**).

The activation energy (E_a) for interfacial K^+ transport (including K^+ through the SEI and K^+ desolvation) was evaluated from temperature-dependent interfacial resistance fitted using the equivalent circuit in Supplementary Fig. 25. The E_a can be calculated based on the Arrhenius equation:

$$\ln\left(\frac{1}{R_{inter.}}\right) = -\frac{E_a}{R} \times \frac{1}{T} + \ln A \quad (3)$$

where R_{inter} is the interfacial resistance of the cells, T is the absolute temperature, R is the standard gas constant, A is the preexponential constant, E_a is the activation energy of interfacial K-ion transport.

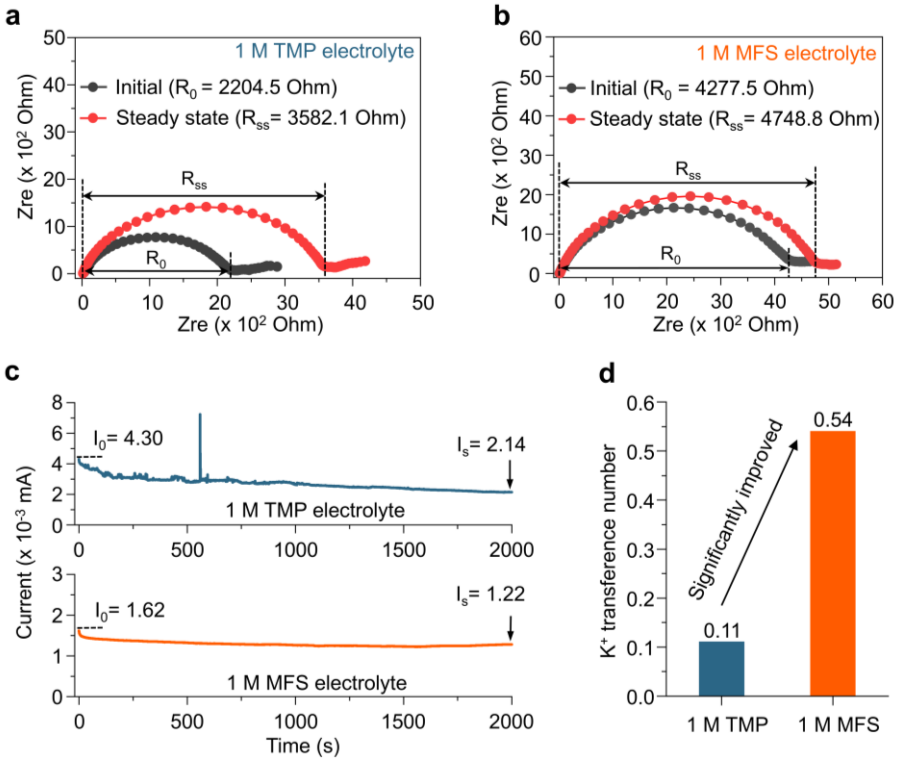

Supplementary Fig. 27. **a**, **b**, Nyquist plots of K-symmetric cells before and after polarization using 1 M TMP (**a**) and 1 M MFS (**b**) electrolytes. **c**, Chronoamperometry profiles of the cells at an applied voltage of 10 mV. **d**, Comparison of the calculated K^+ transference number obtained from the 1 M TMP electrolyte and 1 M MFS electrolyte.

The K^+ transference number (t_{K^+}) was obtained through a combination of

chronoamperometry and impedance spectroscopy analyses using symmetric K cells based on the Bruce-Vincent method.

$$t_{K^+} = \frac{I_{ss}(\Delta V - I_0 R_0)}{I_0(\Delta V - I_{ss} R_{ss})} \quad (4)$$

where I_{ss} represents the steady-state polarization current and I_0 represents the initial-state polarization current. ΔV represents the applied polarization potential. R_{ss} represents the steady-state electrode/electrolyte interfacial resistance and R_0 represents the initial-state electrode/electrolyte interfacial resistance. A small constant polarization potential (10 mV) was applied in the symmetric K cell over 2,000 s.

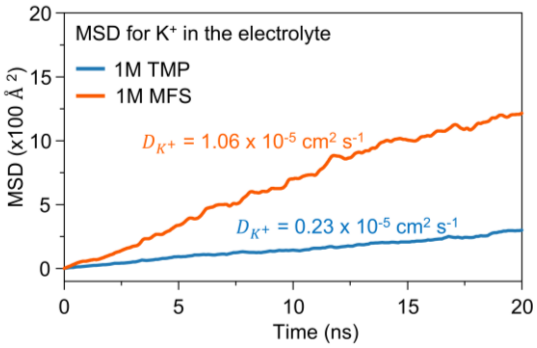

Supplementary Fig. 28. The simulated K^+ diffusion coefficients of the 1 M TMP solution and 1 M MFS solution based on MSD analysis.

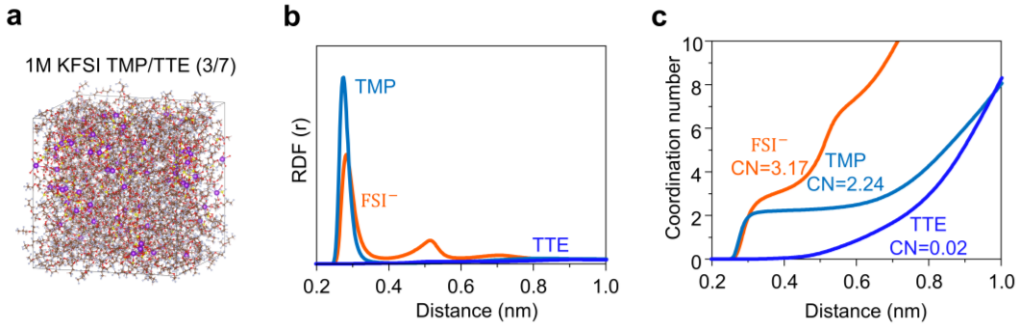

Supplementary Fig. 29. **a**, MD snapshot, **b**, RDF (r), **c**, CN of 1 M KFSI TMP/TTE electrolyte. TTE: 1,1,2,2-tetrafluoroethyl 2,2,3,3-tetrafluoropropyl ether.

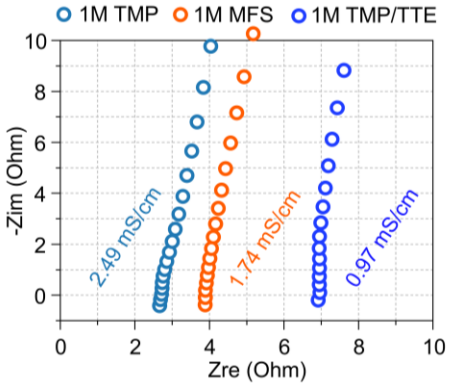

Supplementary Fig. 30. Nyquist plots of various electrolytes. TTE: 1,1,2,2-tetrafluoroethyl 2,2,3,3-tetrafluoropropyl ether.

The stainless steel||stainless steel coin cells to measure the ionic conductivity of the investigated electrolytes in the presence of a separator. The ionic conductivity of the three electrolytes was calculated as:

$$\sigma = \frac{L}{S \times R} \tag{5}$$

where L is the distance between the two pieces of stainless steel, S is the effective area of the stainless steel, and R is the resistance value obtained from electrochemical impedance spectroscopy.

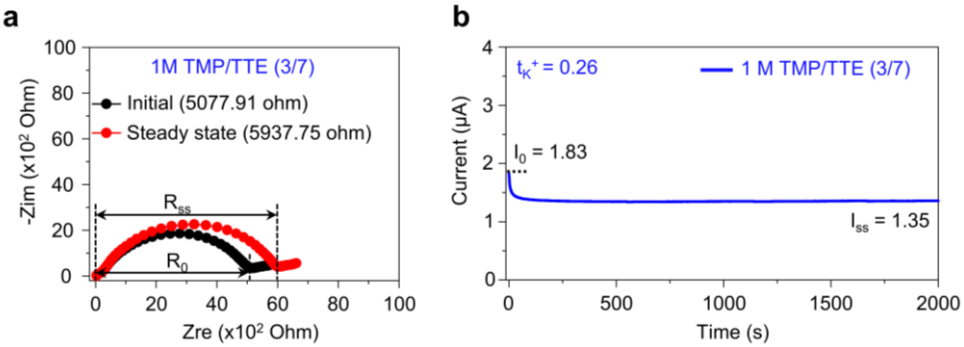

Supplementary Fig. 31. **a**, Nyquist plots of K||K symmetric cell before and after polarization in the 1 M TMP/TTE electrolyte. **b**, Chronoamperometry profiles of the cell at an applied voltage of 10 mV. TTE: 1,1,2,2-tetrafluoroethyl 2,2,3,3-tetrafluoropropyl ether. For conventional localized high-concentration electrolyte (1 M KFSI TMP/TTE), a K^+ transference number of 0.26 is calculated by using the Bruce-Vincent method.

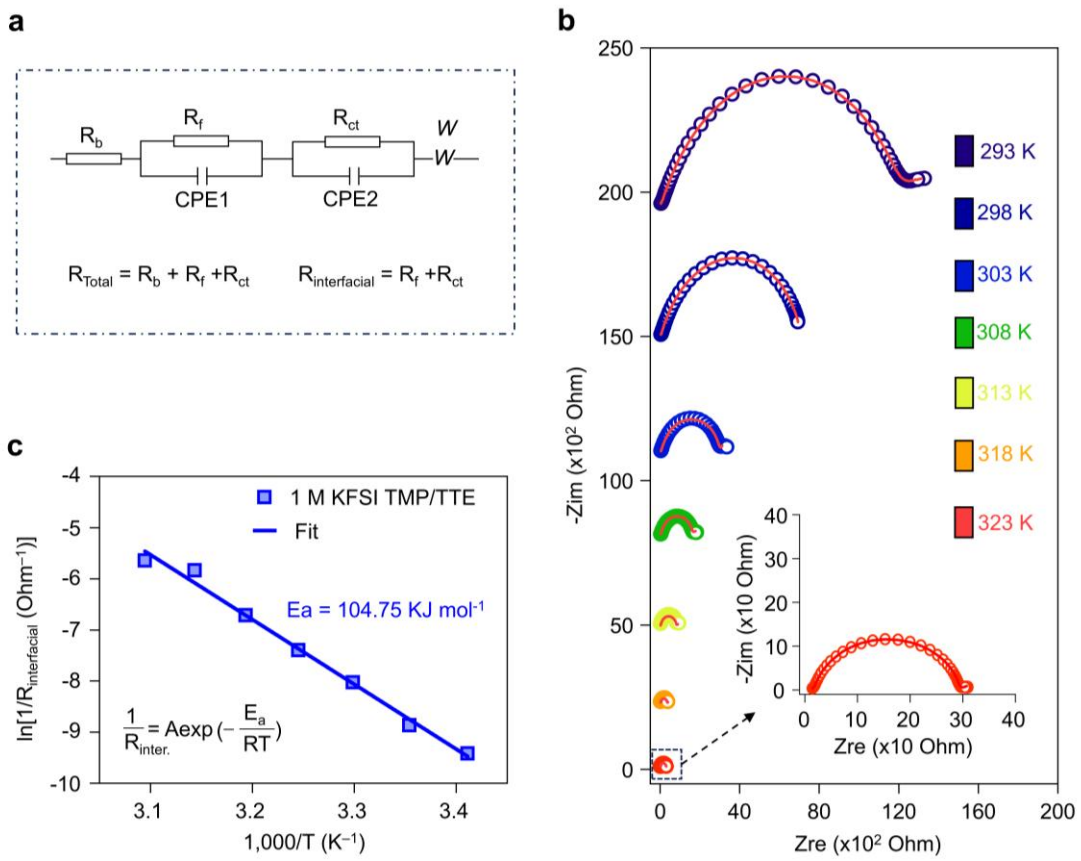

Supplementary Fig. 32. **a**, Equivalent circuit used to fit the Nyquist plots of K||K symmetric cells. **b**, Interfacial resistance of K||K symmetric cells with 1 M KFSI in TMP/TTE measured from 293 to 323 K. **c**, Corresponding activation energy (E_a) for interfacial K-ion transport at the K-metal electrode in the 1 M KFSI TMP/TTE electrolyte.

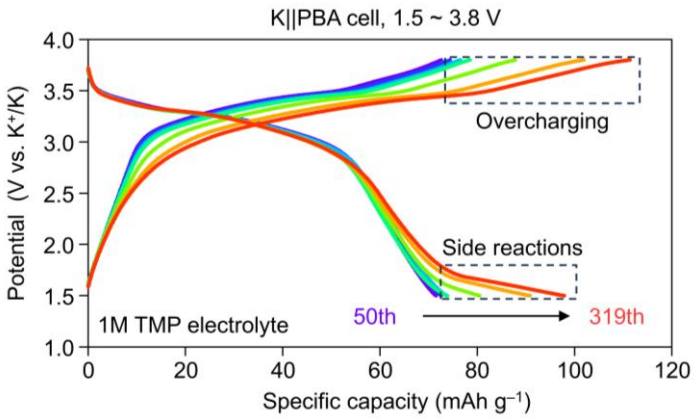

Supplementary Fig. 33. Galvanostatic charge–discharge profiles of K||PBA cells in 1 M TMP electrolyte at 2 C.

As shown in Supplementary Fig. 33, such abnormal charging/discharge behavior of the K||PBA cell stems from the 1 M TMP electrolyte continuous oxidation/reduction, leading to copious CEI/SEI formation and/or extra electrolyte decomposition, which ultimately precipitates rapid battery failure.

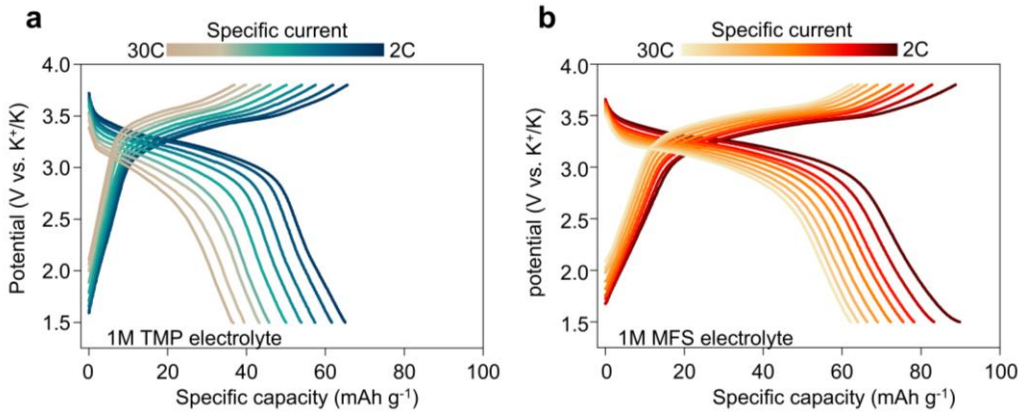

Supplementary Fig. 34. **a**, **b**, Charge–discharge curves of K||PBA cells at different rates in 1 M TMP electrolyte (**a**) and 1 M MFS electrolyte (**b**).

As shown in Supplementary Fig. 34, the voltage polarization could also reflect electrochemical reaction kinetics in the two electrolytes. The rapid increase of charge voltage and decrease of discharge voltage when using the 1 M TMP electrolyte suggest a rapid growth of overpotential due to the slow electrolyte dynamics. By contrast, the cell containing 1 M MFS electrolyte only exhibits a slight increase in polarization voltage under different charging and discharging rates.

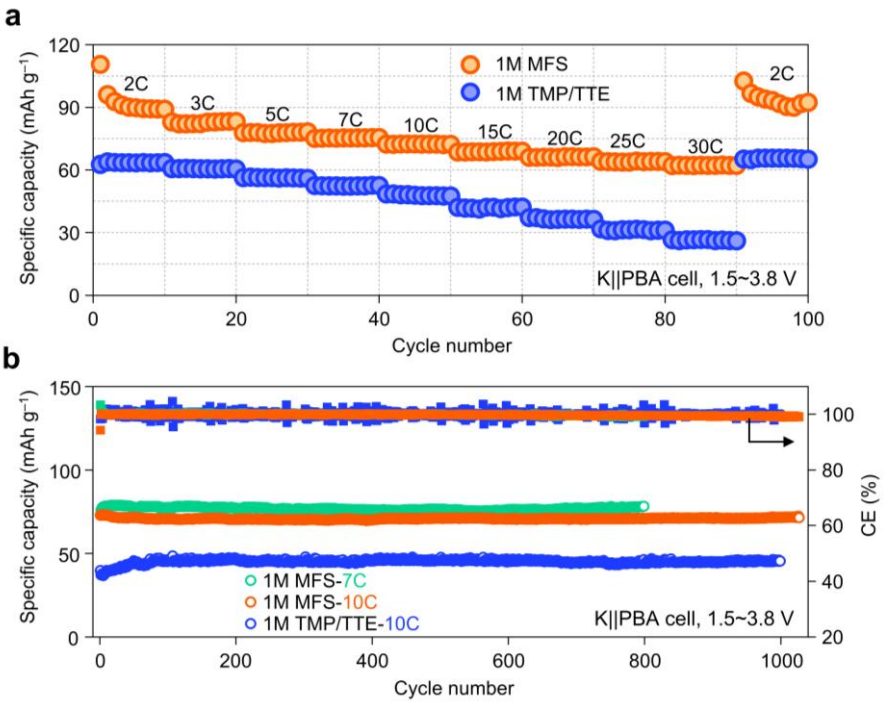

Supplementary Fig. 35. **a**, **b**, Rate performance (**a**) and cycling performance (**b**) of K||PBA cells in 1 M MFS and 1 M TMP/TTE electrolytes.

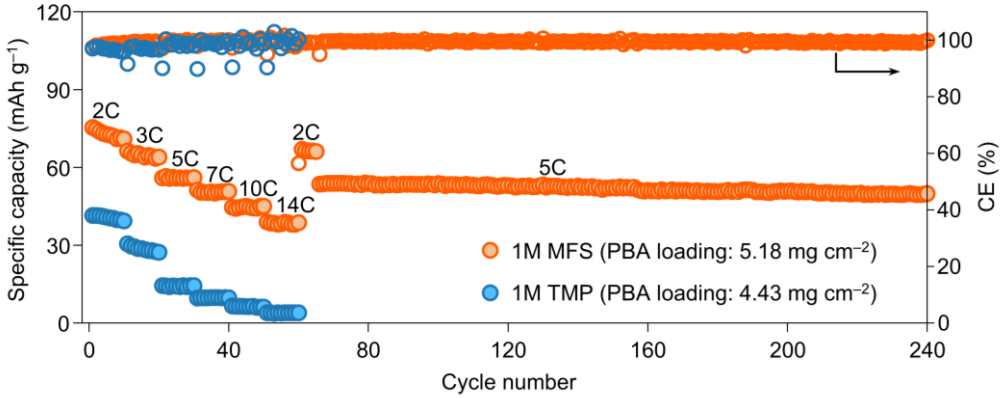

Supplementary Fig. 36. Rate performance of K||PBA cells in 1 M MFS and 1 M TMP electrolytes at high PBA positive electrode loading.

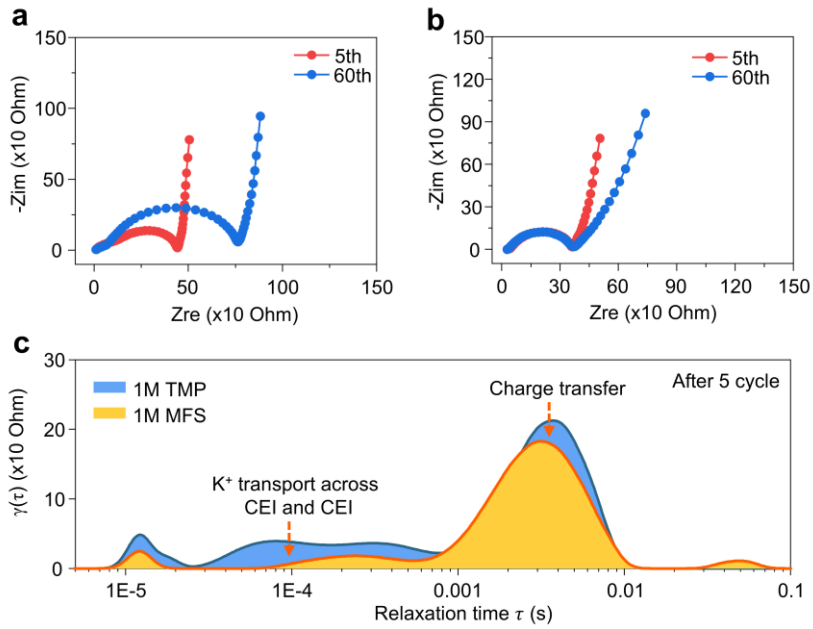

Supplementary Fig. 37. **a**, **b**, Nyquist plots of K||PBA cells after 5 cycles in 1 M TMP electrolyte (**a**) and 1 M MFS electrolyte (**b**). **c**, Distribution of relaxation times (DRT) plots derived from the EIS data of the two electrolytes after 5 cycles.

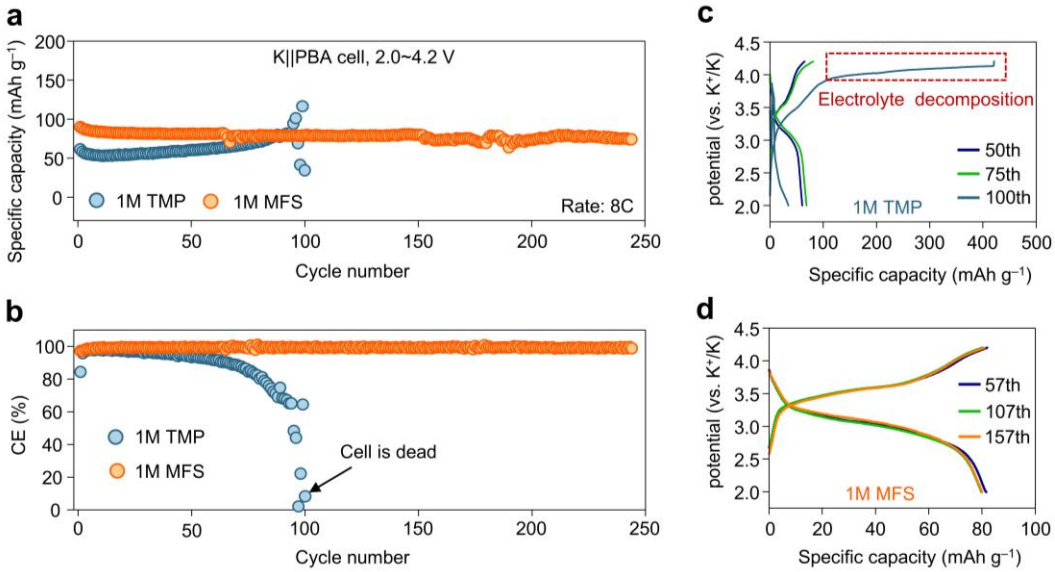

Supplementary Fig. 38. **a**, **b**, Cycling stability (**a**) and CE (**b**) of K||PBA cells in 1 M TMP and 1 M MFS electrolytes. **c**, **d**, Corresponding charge–discharge profiles in the voltage window of 2.0-4.2 V.

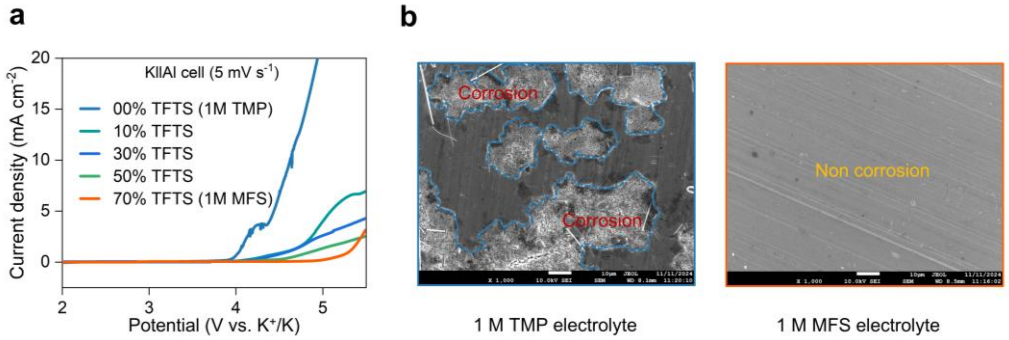

Supplementary Fig. 39. **a**, Linear sweep voltammetry (LSV) curves of K||Al cells in 1 M TMP electrolyte and TFTS-based electrolyte at 25 ℃. **b**, SEM images of the Al current collector after LSV tests in 1 M TMP electrolyte and 1 M MFS electrolyte.

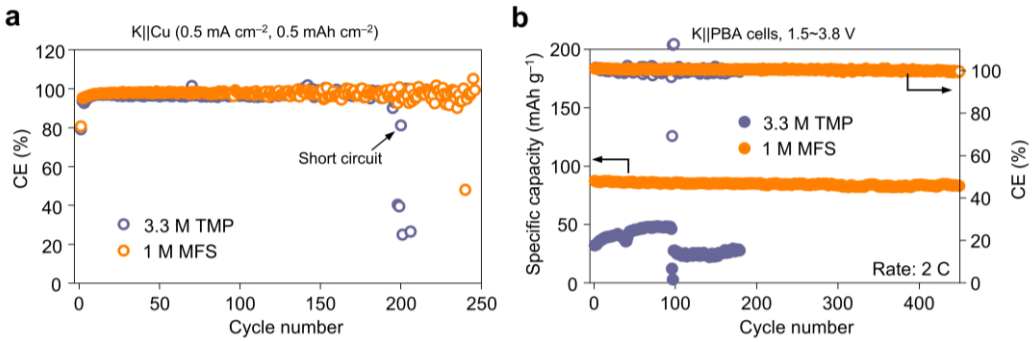

Supplementary Fig. 40. **a**, CE and cycling stability of K||Cu cells in 1 M MFS electrolyte and 3.3 M TMP electrolytes during long-term cycling. **b**, Specific discharge capacity and CE of K||PBA cells in 1 M MFS electrolyte and 3.3 M TMP electrolyte during long-term cycling.

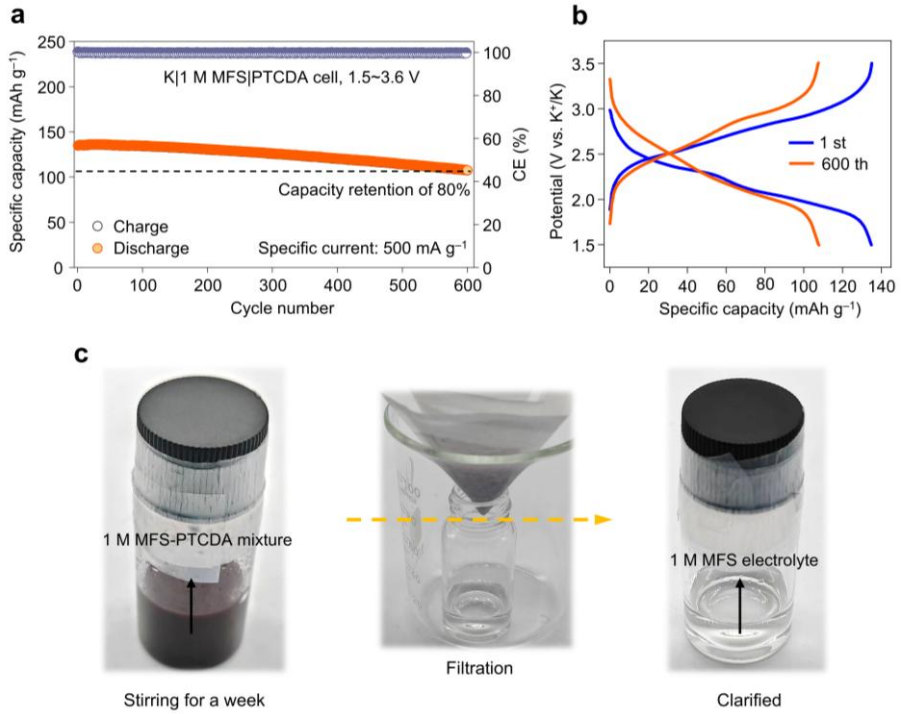

Supplementary Fig. 41. **a**, **b**, Cycling capability (**a**) and corresponding charge-discharge profiles (**b**) of the K||PTCDA cell using 1 M MFS electrolyte at 500 mA g^{-1}. **c**, Optical photographs of the dissolution experiment of PTCDA material in 1 M MFS electrolyte.

As shown in Supplementary Fig. 41c, the filtrate, the mixture of PTCDA powder and 1 M MFS electrolyte after being stirred for a week, remained clear, indicating that the solubility of PTCDA in our 1 M MFS electrolyte was significantly inhibited.

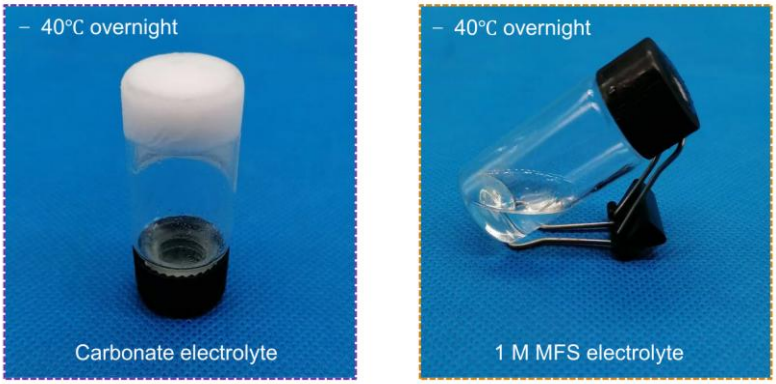

Supplementary Fig. 42. Physical appearances showing the states of carbonate electrolyte and 1 M MFS electrolyte at -40 °C.

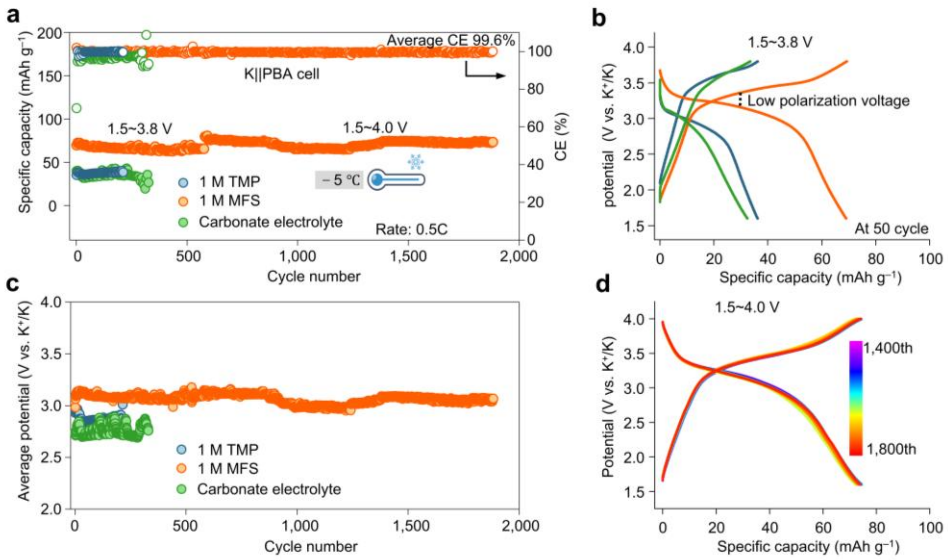

Supplementary Fig. 43. **a**, Cycling performance and CE of K||PBA cells in carbonate electrolyte, 1 M TMP, and 1 M MFS electrolytes at -5 °C. **b**, Charge–discharge profiles of K||PBA cells in the same electrolytes within a voltage range of 1.5–3.8 V at -5 °C. **c**, Average discharge voltage of K||PBA cells in carbonate electrolyte, 1 M TMP, and 1 M MFS electrolytes at -5 °C. **d**, Charge–discharge profiles of K||PBA cells in 1 M MFS electrolyte within a voltage range of 1.5–4.0 V at -5 °C.

As shown in Supplementary Fig. 43, at -5 °C, the K||PBA cell using 1 M MFS electrolyte exhibits higher capacity, better cycling stability, higher average CE (about 99.6%), and reduced voltage polarization, much superior to those with both 1M TMP electrolyte and carbonate-based electrolyte.

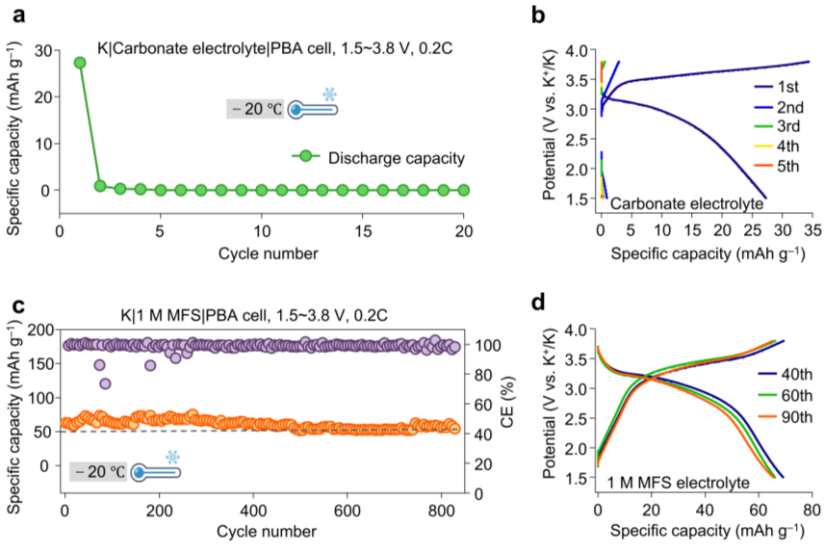

Supplementary Fig. 44. **a**–**d**, Cycling stability and corresponding charge–discharge curves of K||PBA cells in carbonate electrolyte (**a**, **b**) and 1 M MFS electrolyte (**c**, **d**) at -20 ± 2 °C.

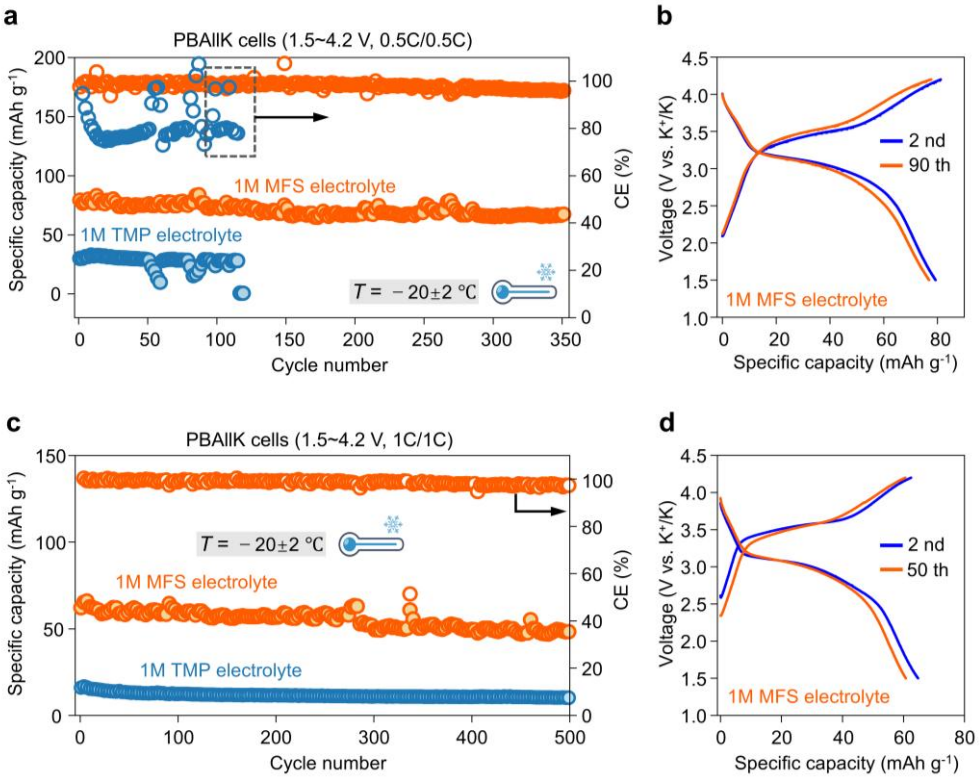

Supplementary Fig. 45. **a-d**, Cycling performance of K||PBA cells in 1 M TMP and 1 M MFS electrolytes at 0.5 C (**a**) and 1 C (**c**), and corresponding charge–discharge curves in 1 M MFS electrolyte at 0.5 C (**b**) and 1 C (**d**), at -20 ± 2 °C.

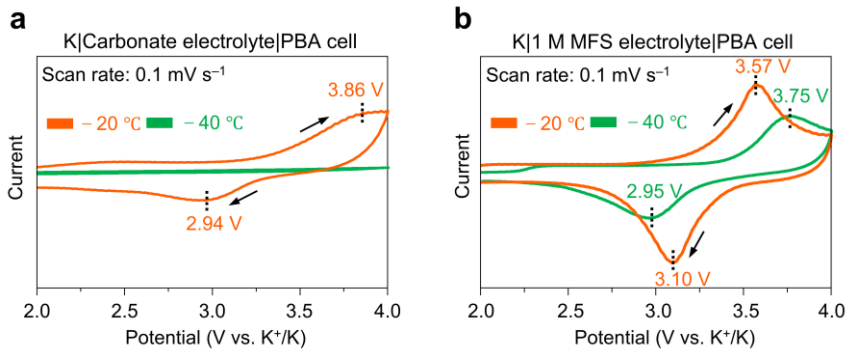

Supplementary Fig. 46. **a**, **b**, Cyclic voltammetry (CV) curves of K||PBA cells at different extreme temperatures in carbonate electrolyte (**a**) and 1 M MFS electrolyte (**b**).

Supplementary Fig. 46 shows the CV curves of K||PBA cells in carbonate electrolyte and 1 M MFS electrolyte at two low temperatures. In the cells with carbonate electrolyte, no pronounced redox peaks are observed in the CV profiles when the temperature decreases to -20 °C and -40 °C, likely due to the solidification of the electrolyte, which hinders normal K^+ transport and prevents the PBA electrode from fully participating in the charge–discharge process. In contrast, well-defined and symmetric redox peaks are observed for the PBA positive electrode in 1 M MFS electrolyte even at -40 °C, although the overpotential increases due to the reduced K^+ diffusion kinetics at extremely low temperatures. These results demonstrate that the 1 M MFS electrolyte exhibits good interfacial stability with the electrode and maintains excellent low-temperature electrochemical performance.

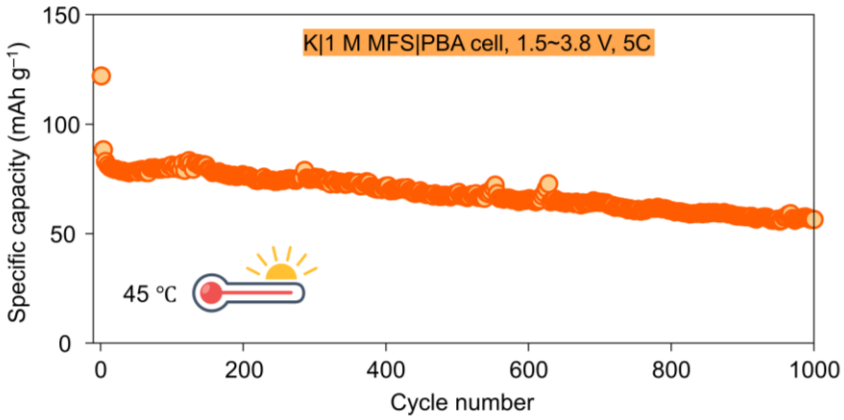

Supplementary Fig. 47. Cycling stability of K||PBA cells in 1 M MFS electrolyte at 45 °C.

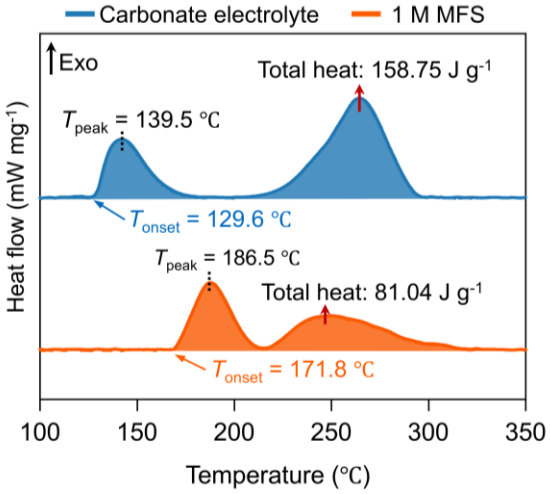

Supplementary Fig. 48. DSC analysis of charged PBA positive electrode (4.2 V vs. K^+/K) mixed with the relevant carbonate electrolyte and 1 M MFS electrolyte.

As shown in Supplementary Fig. 48, DSC analysis of electrolyte-PBA mixtures (charged to 4.2 V) revealed that both electrolytes exhibited two exothermic peak, which could be attributed the decomposition of CEI and PBA positive electrode and the reaction between the charged PBA positive electrode and the electrolyte, while 1M MFS electrolyte showed a significantly higher onset temperature ($T_{\mathrm{onset}} = 171.8$ °C) for exothermic decomposition compared to carbonate electrolyte ($T_{\mathrm{onset}} = 129.6$ °C). More importantly, the total heat release for those exothermic reactions in 1M MFS electrolyte dropped to 81.04 J g^{-1}, equal to 51% of that in carbonate electrolyte (158.75

J g^{-1}). These results indicate that thermal reactions are strongly suppressed in 1 M MFS electrolyte, which is beneficial for mitigating battery safety risks under thermal runaway conditions.

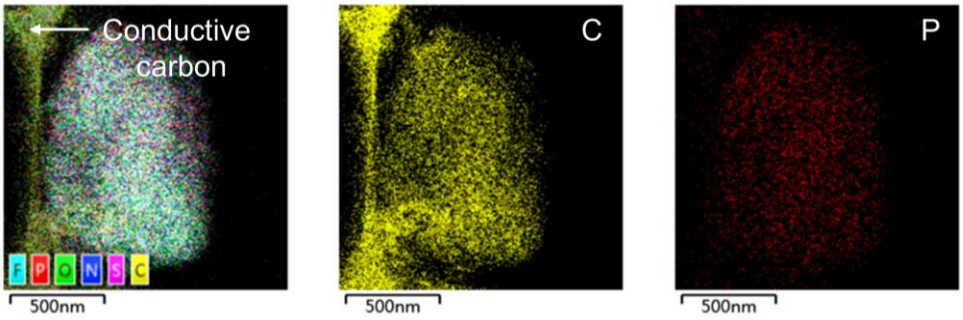

Supplementary Fig. 49. EDS mapping of the cycled PBA positive electrode in 1 M MFS electrolyte, obtained by scanning transmission electron microscopy (STEM).

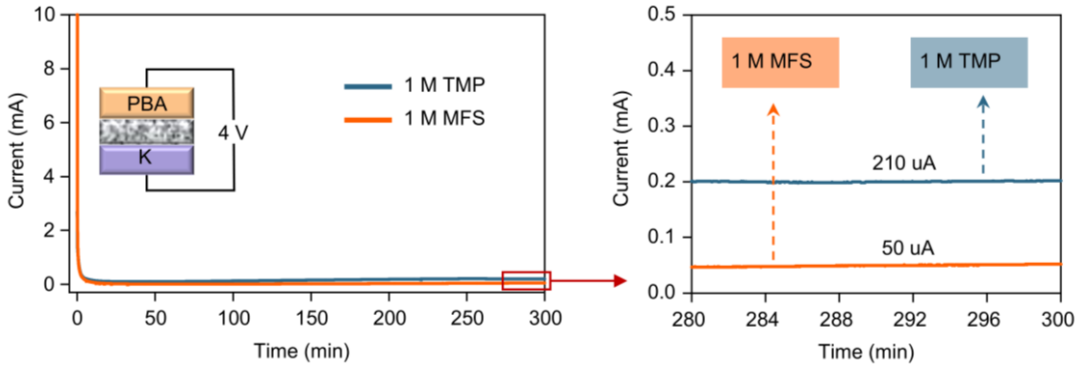

Supplementary Fig. 50. Leakage current of PBA positive electrodes during a constant-voltage floating test at 4.0 V after CEI formation in 1 M TMP and 1 M MFS electrolytes.

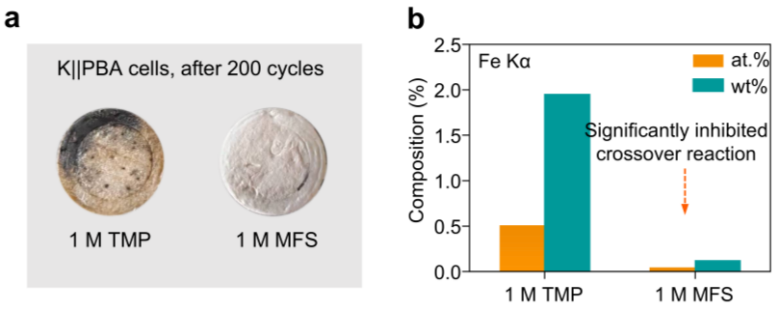

Supplementary Fig. 51. **a**, **b**, Photographs of K||PBA cell separators after 200 cycles (**a**) and the amount of transition metal (Fe) deposited on cycled K-metal negative electrodes after 200 cycles in 1 M TMP and 1 M MFS electrolytes, as determined by energy-dispersive X-ray spectroscopy (Fe Kα) (**b**).

After disassembling the cells following cycling, it was observed that the separator from the cell with 1 M TMP electrolyte exhibited an abnormal yellow coloration, suggesting electrolyte decomposition and Fe dissolution (Supplementary Fig. 51a). In addition, several black regions were observed on the separator in the TMP cell, indicative of minor burning caused by an internal short circuit. The formation of unstable interfaces at both the positive and negative electrodes in TMP electrolyte is a plausible explanation for these phenomena. In sharp contrast, the separator extracted from cells with 1 M MFS electrolyte remained white, demonstrating that this electrolyte provides exceptional interfacial stability with both electrodes. These observations help explain the superior electrochemical performance of cells utilizing 1 M MFS electrolyte. Notably, Fe dissolution can induce crosstalk with the negative electrode in a full-cell configuration. Quantitative analysis of the deposited Fe species was performed via SEM-EDS (Supplementary Fig. 51b), revealing that after 200 cycles, the Fe content on the K-metal negative electrode is markedly lower in cells cycled with 1 M MFS electrolyte than in those cycled with 1 M TMP electrolyte.

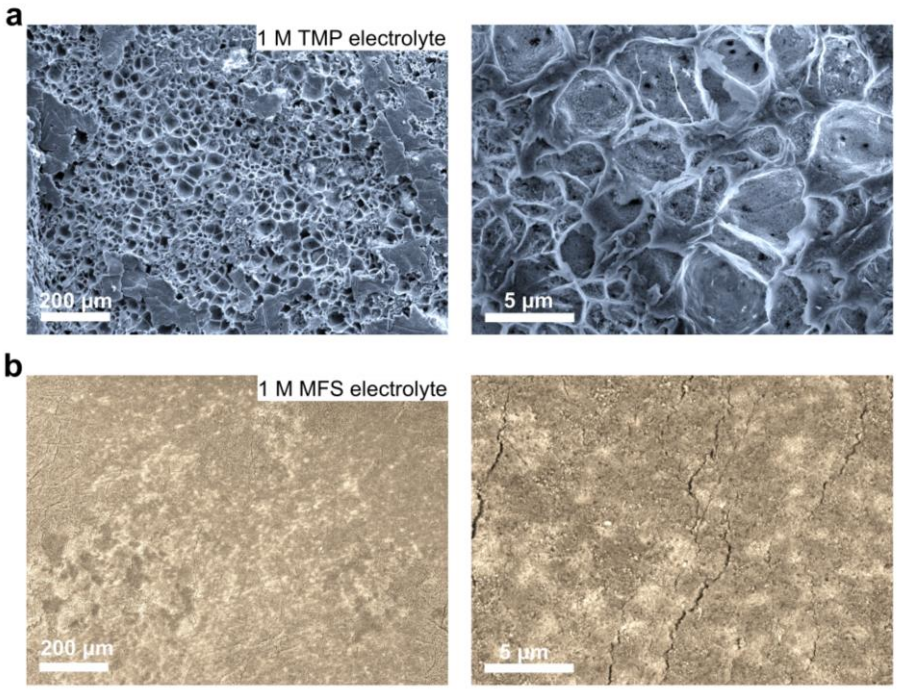

Supplementary Fig. 52. **a**, **b**, Surface SEM images of K-metal electrode in K||PBA cells with 1 M TMP electrolyte (**a**) and 1 M MFS electrolyte (**b**) after 200 cycles at 2 C.

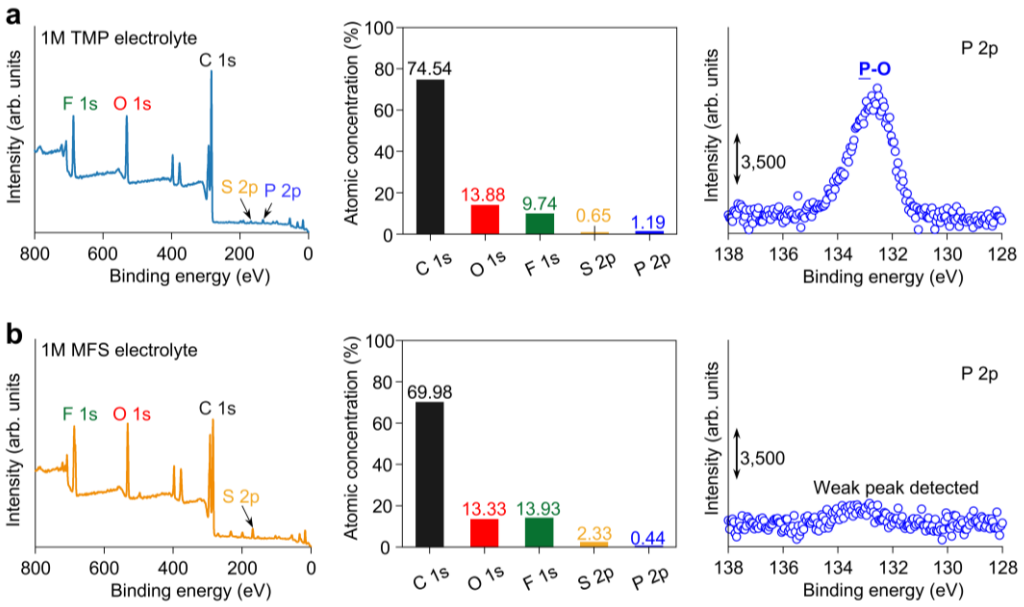

Supplementary Fig. 53. **a**, **b**, XPS surveys, atomic ratios, and high-resolution P 2p spectra of the CEI layer formed on PBA electrodes cycled in 1 M TMP (**a**) and 1 M MFS (**b**) electrolytes. Spectra were recorded from the PBA electrode surface after 5 cycles.

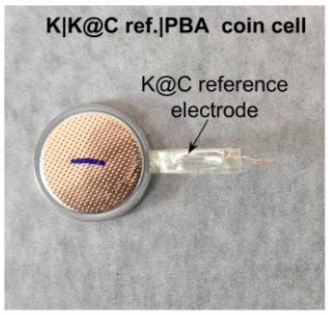

Supplementary Fig. 54. Optical photograph of a three-electrode K|K@C ref.|PBA coin cell. In this cell, PBA served as the working electrode, K-metal served as the counter electrode, and K@C served as the reference electrode.

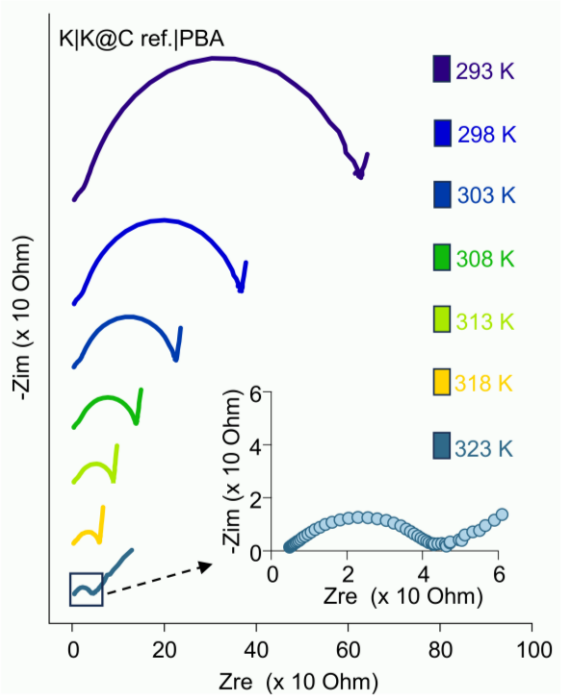

Supplementary Fig. 55. Temperature-dependent EIS measurements of the three-electrode K|K@C ref.|PBA cell with 1 M TMP electrolyte (Inset: expansion of the boxed region).

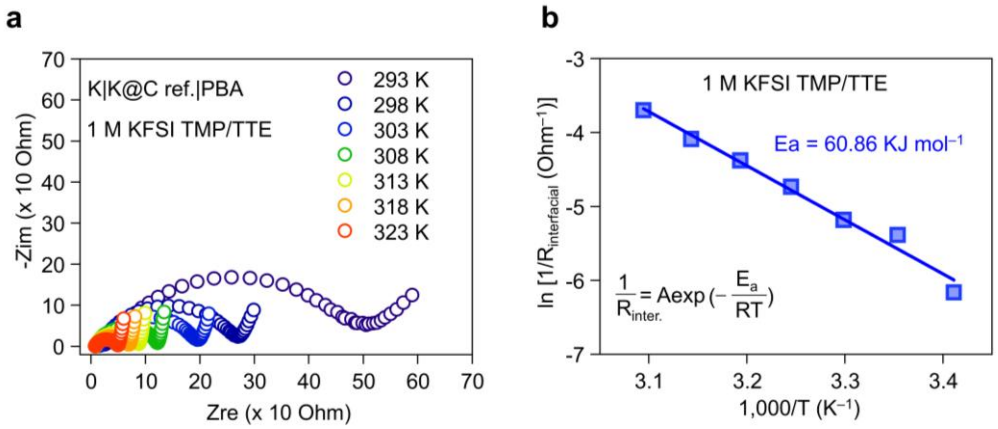

Supplementary Fig. 56. **a**, **b**, Resistance measurements of a three-electrode K|K@C ref.|PBA cell at 293–323 K (**a**) and the corresponding activation energy (E_a) for interfacial K-ion transport on the PBA electrode in 1 M TMP/TTE electrolyte (**b**).

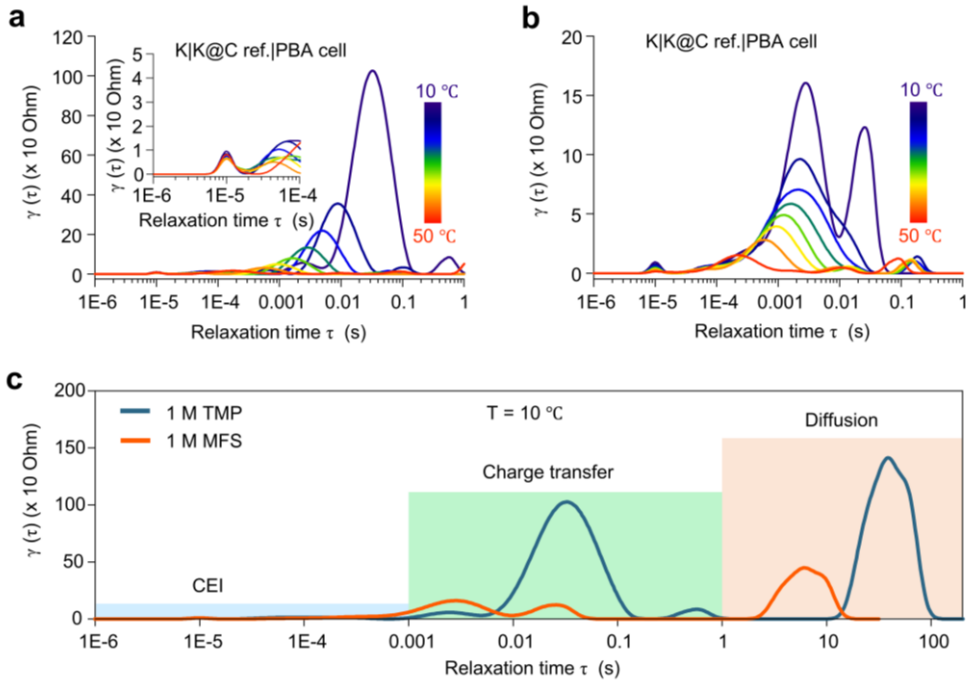

Supplementary Fig. 57. **a**–**c**, Temperature-dependent DRT plots derived from EIS data from a three-electrode K|K@C ref.|PBA cell in 1 M TMP (**a**) and 1 M MFS (**b**) electrolytes, and the corresponding distribution of DRT profiles at 10 °C in the two electrolytes (**c**).

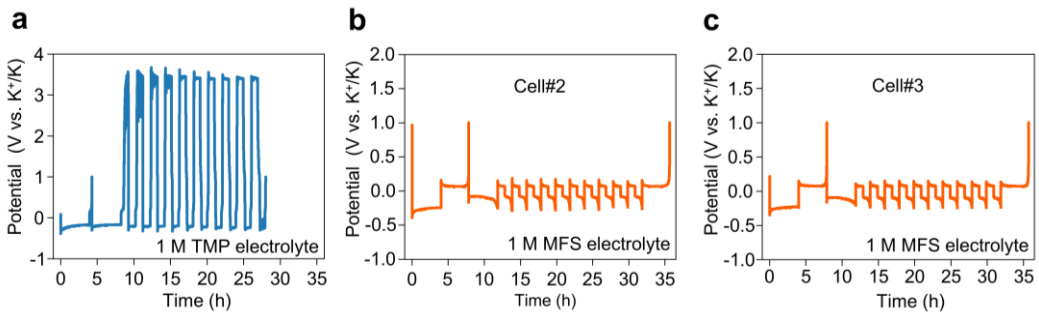

Supplementary Fig. 58. **a**–**c**, CE of K-metal plating/stripping in 1 M TMP (**a**) and 1 M MFS (**b**, **c**) electrolytes, measured using the Aurbach protocol.

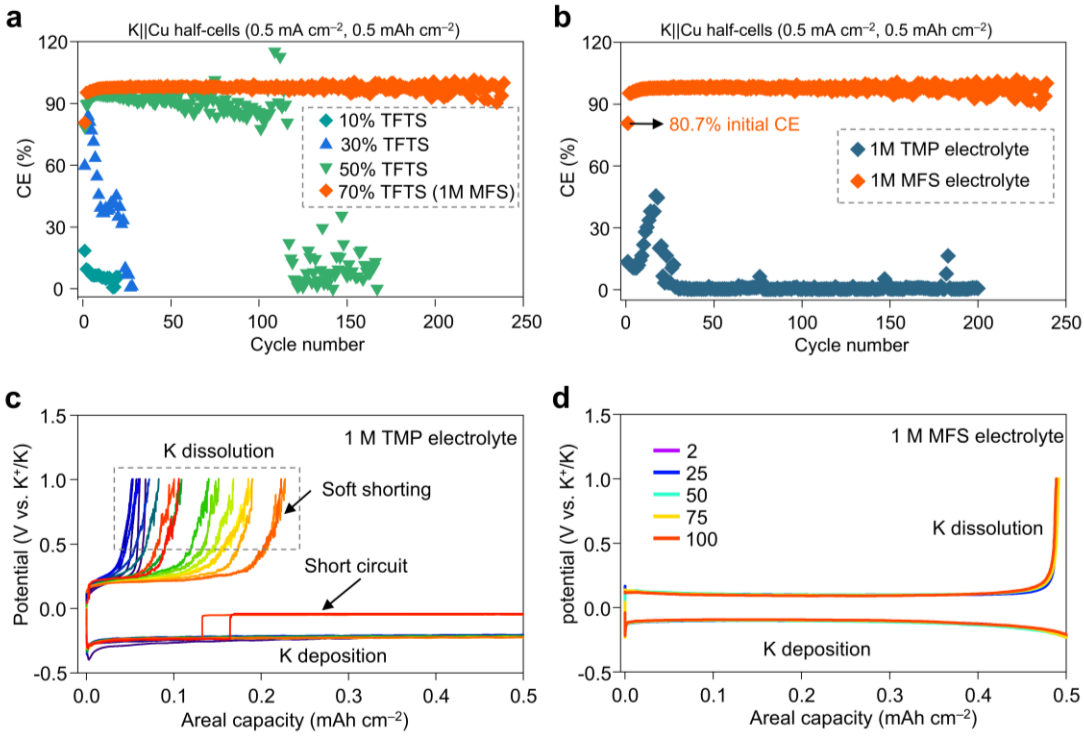

Supplementary Fig. 59. **a**–**d**, CE and cycling performance of K||Cu cells in TFTS-based and 1 M TMP electrolytes (**a**, **b**), and charge–discharge curves of K deposition and dissolution in 1 M TMP (**c**) and 1 M MFS (**d**) electrolytes.

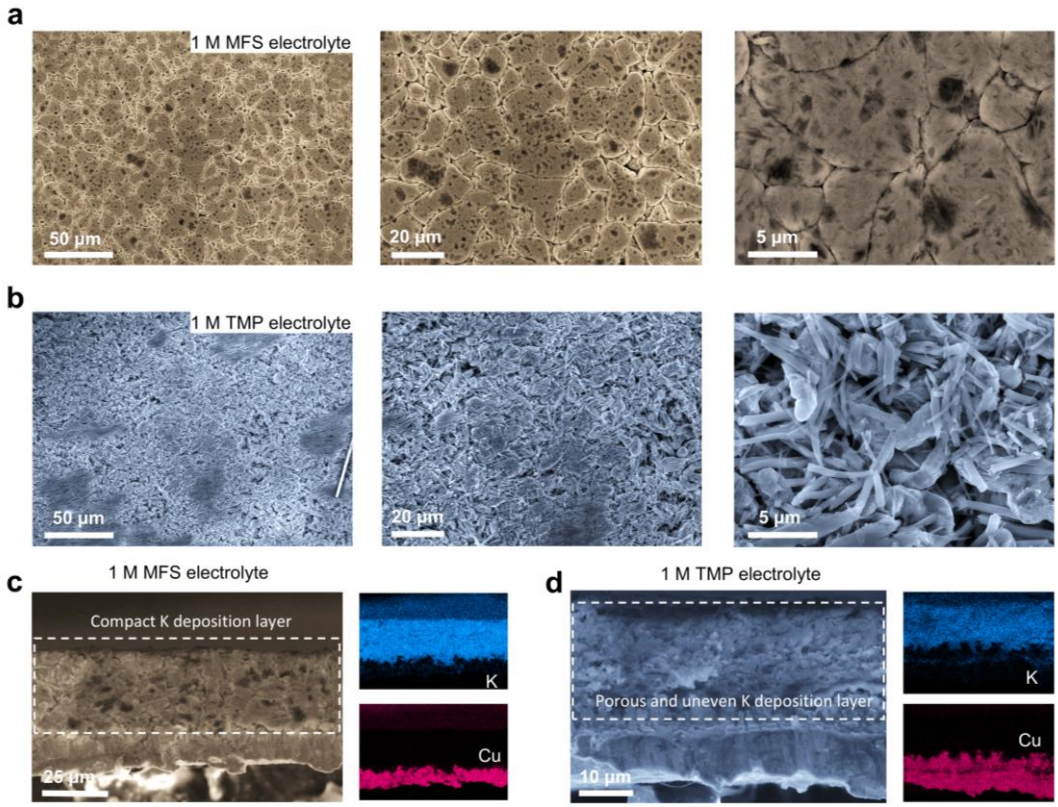

Supplementary Fig. 60. **a-d**, Top-view and cross-sectional SEM images of K plating morphologies on Cu substrates in 1 M MFS (**a**, **c**) and 1 M TMP (**b**, **d**) electrolytes at 0.5 mA cm^{-2} and 2 mAh cm^{-2}.

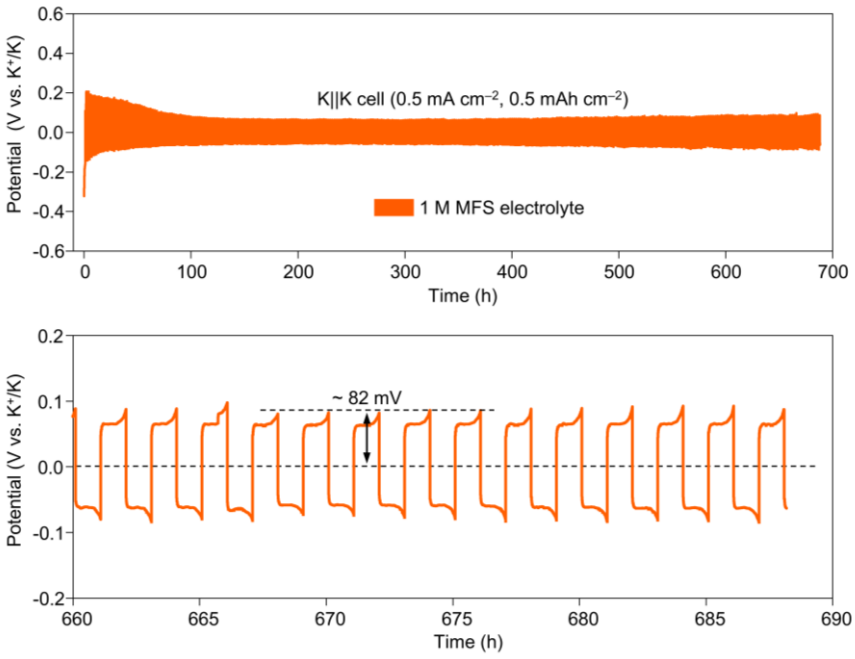

Supplementary Fig. 61. Cycling performance of K||K symmetric cells in 1 M MFS electrolyte at 0.5 mA cm^{-2} and 0.5 mAh cm^{-2}.

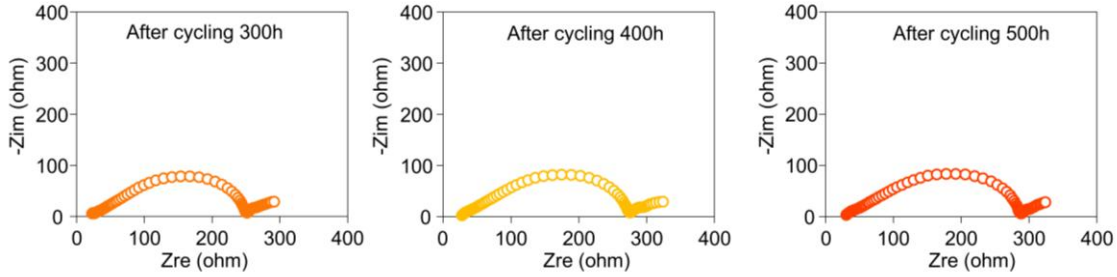

Supplementary Fig. 62. Nyquist plots of K||K symmetric cells in 1 M MFS electrolyte at different cycles and a current density of 0.5 mA cm^{-2} with a capacity of 0.25 mAh cm^{-2}.

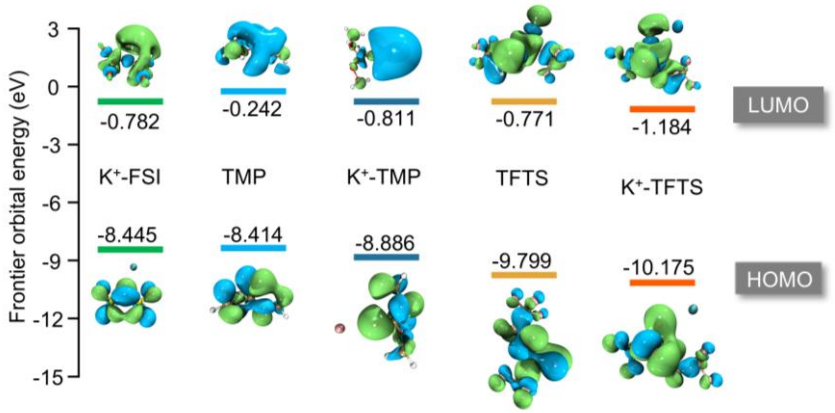

Supplementary Fig. 63. Frontier molecular orbital energy diagrams and levels of solvents, K^+-FSI^-, and K^+-solvent complexes in 1 M MFS electrolyte.

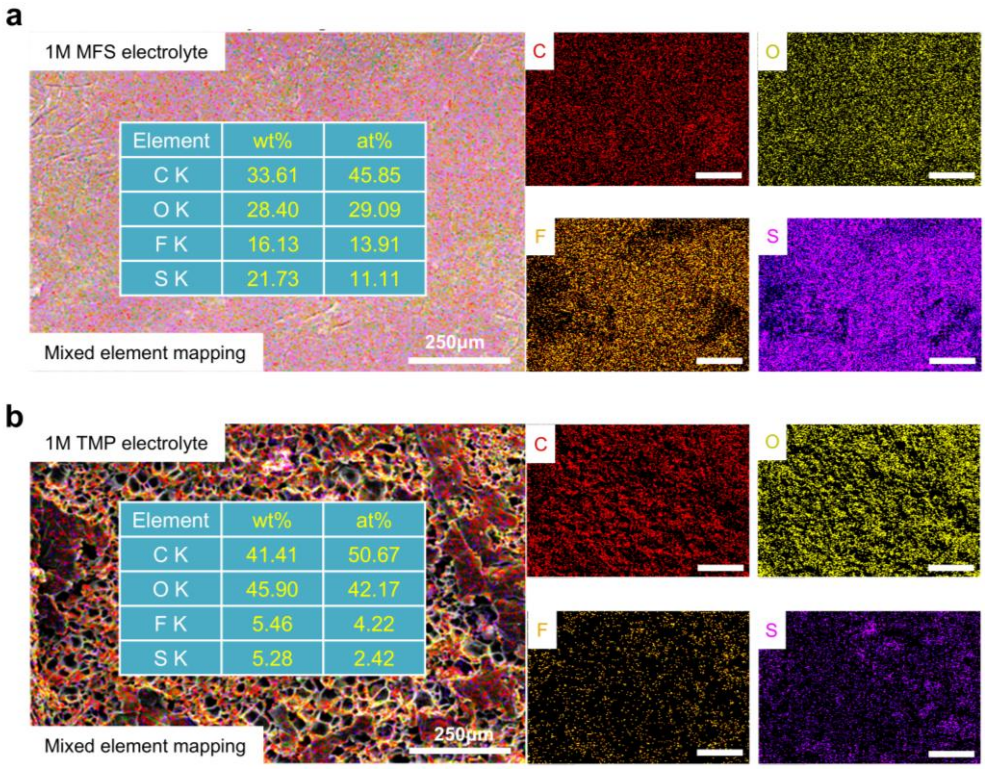

Supplementary Fig. 64. **a**, **b**, SEM/EDS of the cycled K-metal negative electrode in K||PBA coin cells using 1 M MFS (**a**) and 1 M TMP (**b**) electrolytes.

As shown in Supplementary Fig. 64, the SEI formed on the K-metal negative electrode surface in the developed 1 M MFS electrolyte exhibits an apparently higher atomic concentration ratio of F and S than that of the 1 M TMP electrolyte, supporting the formation of a F, S-rich SEI on the K-metal negative electrode.

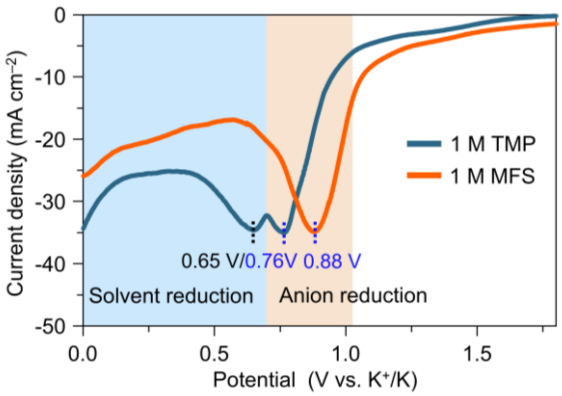

Supplementary Fig. 65. LSV curves of K||Cu asymmetric cells in 1 M TMP electrolyte and 1 M MFS electrolyte.

As shown in Supplementary Fig. 65, the interfacial reaction behaviour of the electrolyte was investigated using LSV curve in the K||Cu half cells. The blue and orange regions in low and high-voltage regions correspond to solvent and anion reduction, respectively. For 1 M MFS electrolyte, a sharp current peak centered at 0.88 V is ascribed to the decomposition of the FSI^- anions, and it shifts toward higher potentials compared to the 1 M TMP electrolyte (at 0.76 V). This can be attributed to the formation of anion-rich solvation structures in the 1 M MFS electrolyte, which increases the reduction potential of anions. The formation of inorganic-rich species (such as KF) at the interface from the reduction of the FSI^- anions inhibit the reduction of solvents in following cathodic scans region (blue) as demonstrated by the decreases of the current density. By contrast, the K||Cu cells with the 1 M TMP electrolyte shows broad shoulder peaks associated with TMP degradation and FSI^- anions reduction (0.65 V to 0.76 V), reaching a high reduction current density for solvent decomposition associated with the formation of thick and highly electronic conductive organic-rich SEI film.

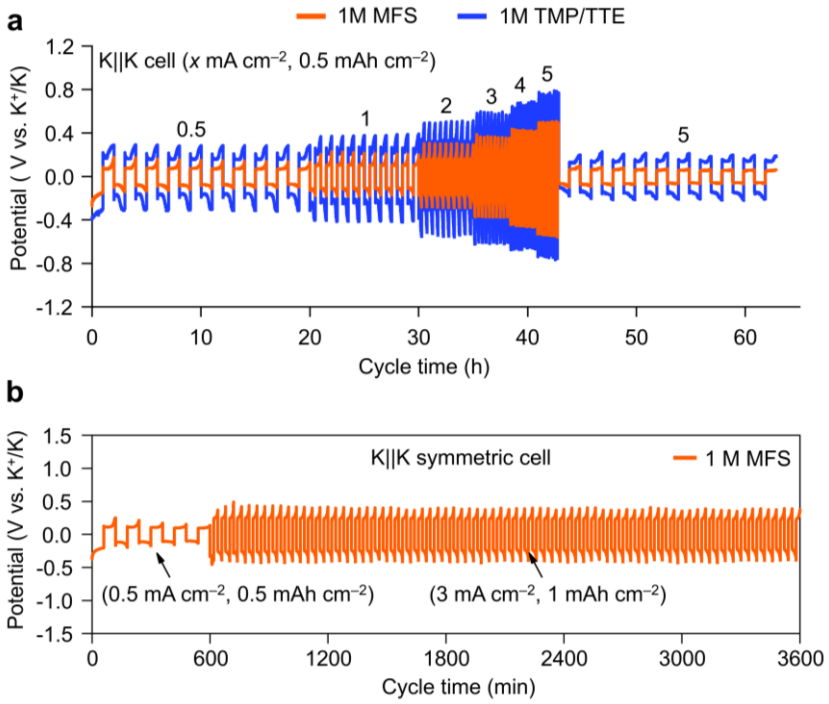

Supplementary Fig. 66. **a**, **b**, Rate capability of K||K symmetric cells in 1 M MFS and 1 M TMP/TTE electrolytes (**a**) and cycling performance of K||K symmetric cells in 1 M MFS electrolyte (**b**) at 3 mA cm^{-2} and 1 mAh cm^{-2}.

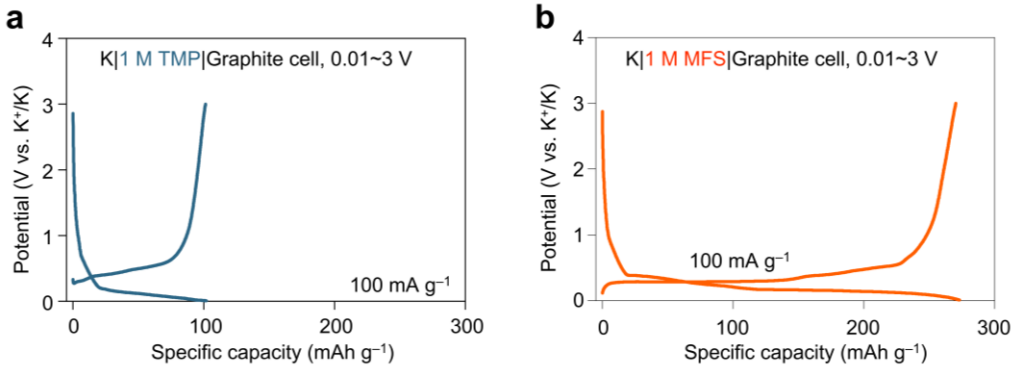

Supplementary Fig. 67. **a**, **b**, Charge–discharge curves of the graphite negative electrode in 1 M TMP electrolyte (**a**) and 1 M MFS electrolyte (**b**).

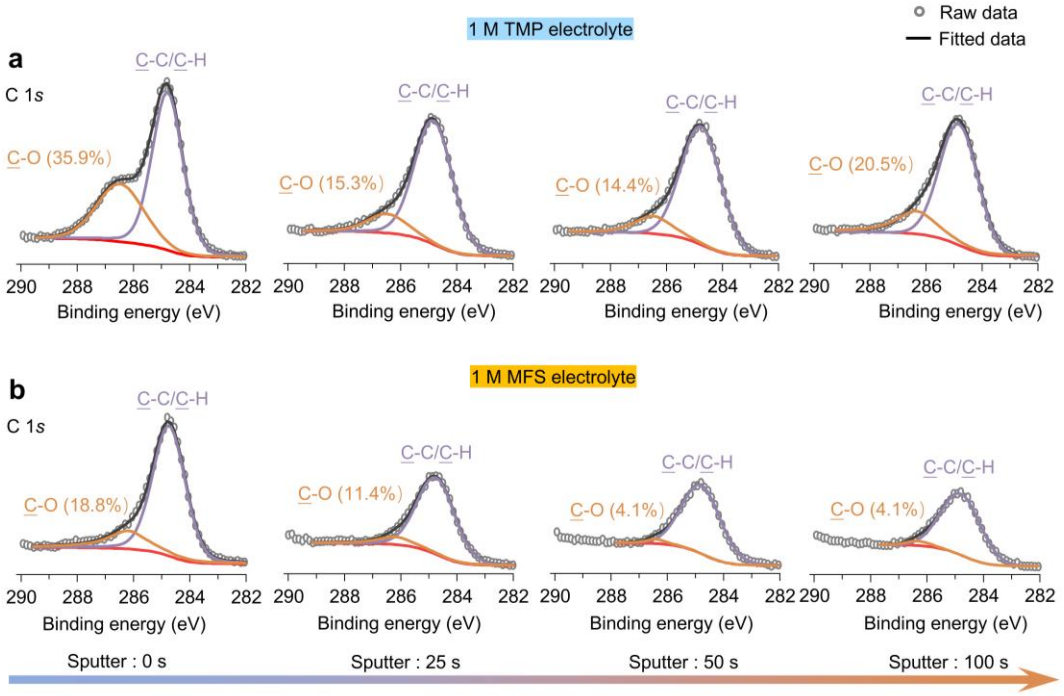

Supplementary Fig. 68. **a**, **b**, High-resolution C 1*s* XPS spectra of the SEI formed on the graphite electrode surface in Graphite||K cells at 100 mA g^{-1} after 20 cycles and 28 ± 1 °C with 1 M TMP (**a**) and 1 M MFS (**b**) electrolytes.

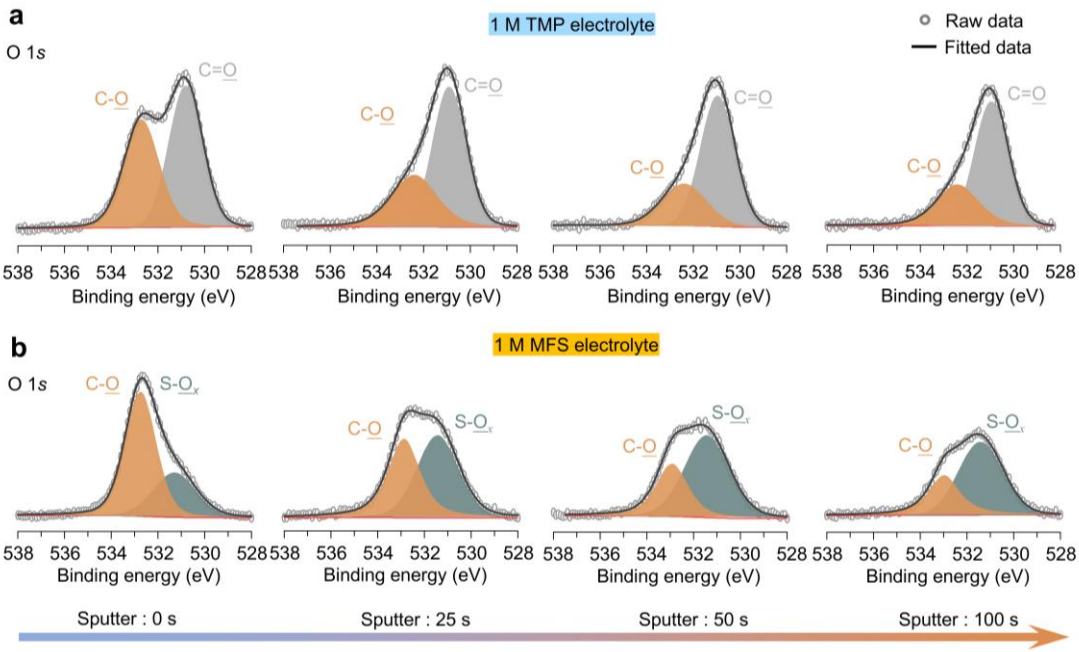

Supplementary Fig. 69. **a**, **b**, High-resolution O 1*s* XPS spectra of the SEI formed on the graphite electrode surface in Graphite||K cells at 100 mA g^{-1} after 20 cycles and 28 ± 1 °C with 1 M TMP (**a**) and 1 M MFS (**b**) electrolytes.

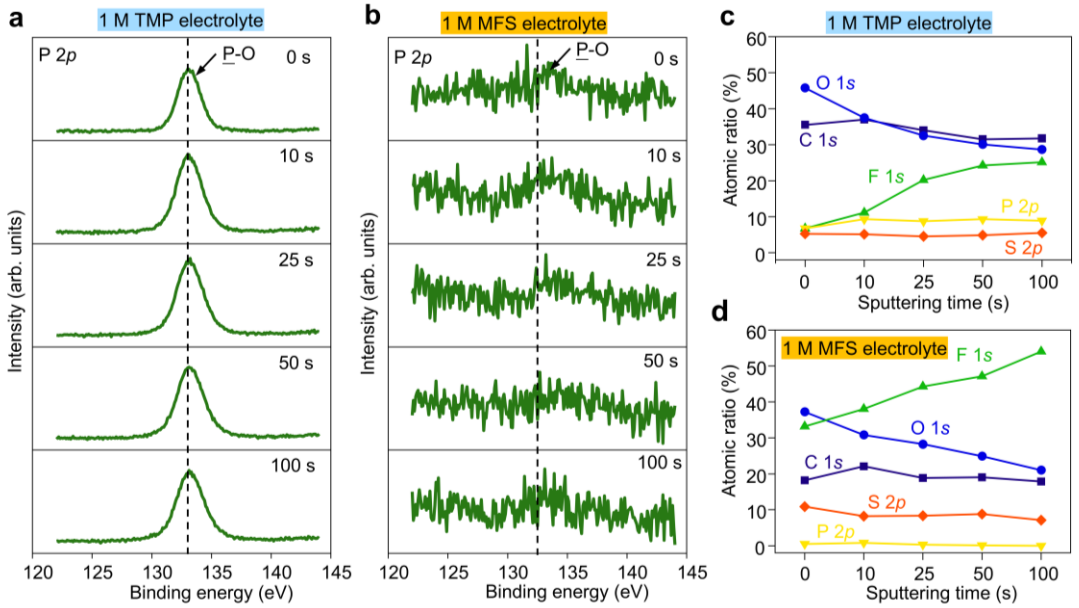

Supplementary Fig. 70. **a**, **b**, High-resolution P 2*p* XPS spectra of the SEI formed on the graphite electrode surface in Graphite||K cells at 100 mA g^{-1} after 20 cycles and 28 ± 1 °C with 1 M TMP (**a**) and 1 M MFS (**b**) electrolytes. **c**, **d**, Atomic ratio distributions from XPS for the SEI on the graphite electrode surface cycled in 1 M TMP (**c**) and 1 M MFS (**d**) electrolytes.

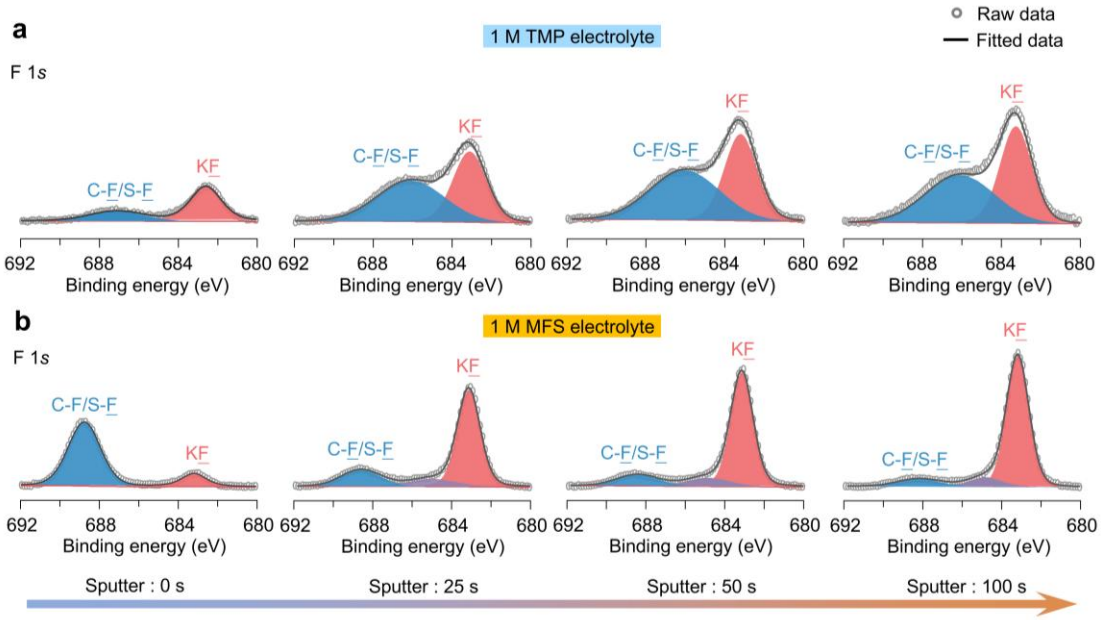

Supplementary Fig. 71. **a**, **b**, High-resolution F 1*s* XPS spectra of the SEI formed on the graphite electrode surface in Graphite||K cells at 100 mA g^{-1} after 20 cycles and 28 ± 1 °C with 1 M TMP (**a**) and 1 M MFS (**b**) electrolytes.

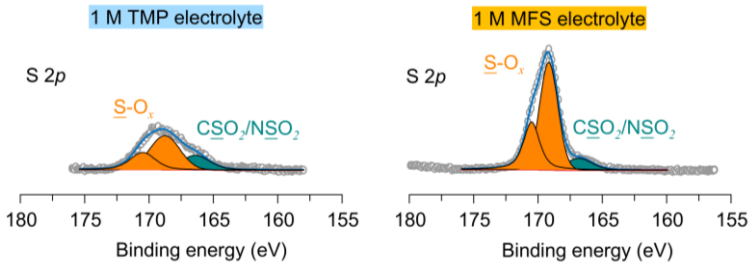

Supplementary Fig. 72. High-resolution S 2*p* XPS spectra of the SEI formed on the graphite electrode surface (100 mA g^{-1}, after 20 cycles, 28 ± 1 °C) in Graphite||K cells with 1 M TMP and 1 M MFS electrolytes.

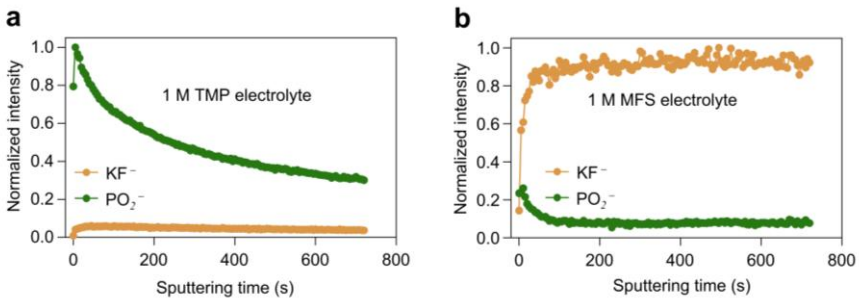

Supplementary Fig. 73. **a**, **b**, TOF-SIMS depth analysis of the SEI formed on the cycled graphite electrode in Graphite||K cells at 100 mA g^{-1} after 20 cycles and 28 ± 1 °C with 1 M TMP (**a**) and 1 M MFS (**b**) electrolytes.

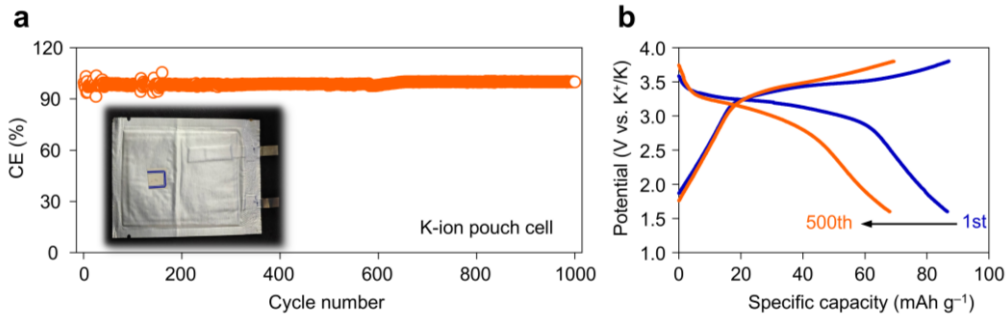

Supplementary Fig. 74. **a**, **b**, CE (**a**) and corresponding charge–discharge curves (**b**) of K-ion pouch cells.

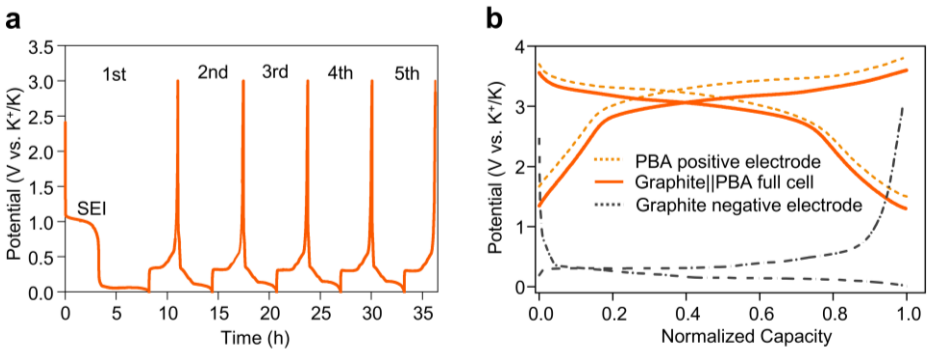

Supplementary Fig. 75. **a**, Voltage–time profiles of the graphite negative electrode in 1 M MFS electrolyte at 100 mA g^{-1}. **b**, Normalized charge-discharge profiles of the graphite negative electrode and PBA positive electrode in half-cells, and the corresponding profile of Graphite||PBA full cell in 1 M MFS electrolyte.

Before full cell assembly, the graphite negative electrode was first cycled in a half-cell against a K-metal electrode to form a stable SEI and eliminate irreversible capacity loss (Supplementary Fig. 75a).

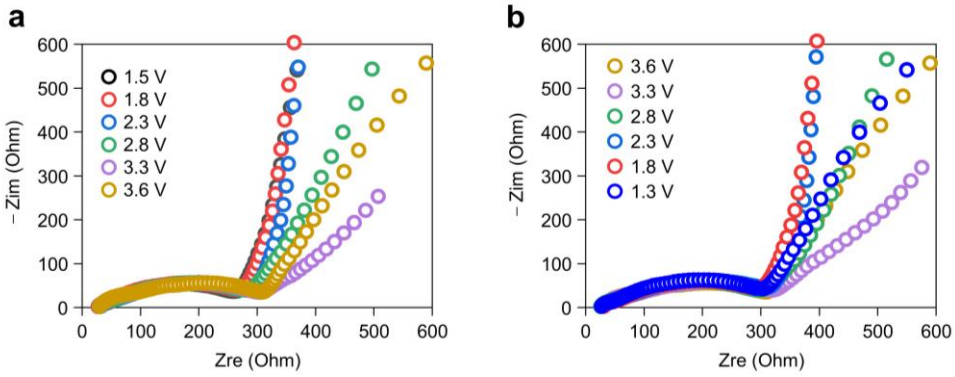

Supplementary Fig. 76. **a**, **b**, Impedance evolution of the Graphite||PBA full cell during charging (**a**) and discharging (**b**) at 2 C.

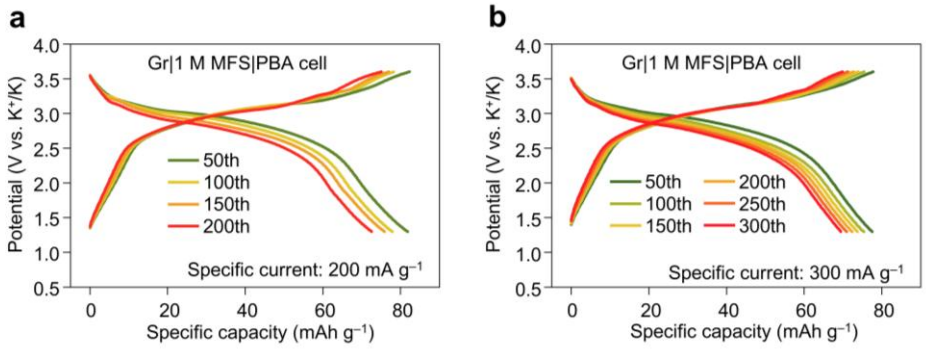

Supplementary Fig. 77. **a**, **b**, Charge–discharge curves of the Graphite||PBA full cell in 1 M MFS electrolyte at 200 mA g^{-1} (**a**) and 300 mA g^{-1} (**b**).

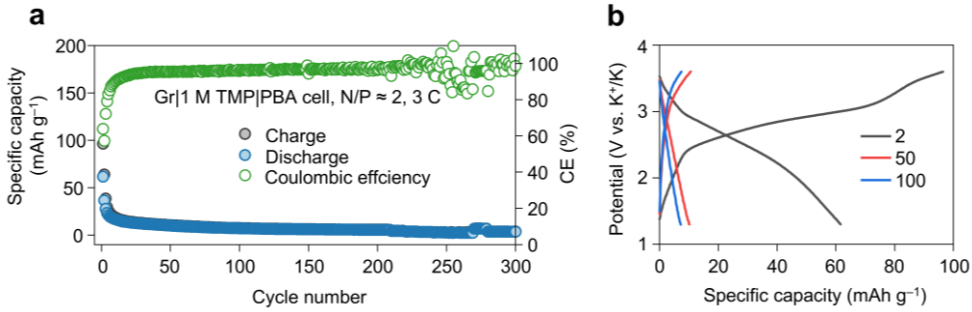

Supplementary Fig. 78. **a**, **b**, Cycling performance (**a**) and corresponding charge–discharge curves (**b**) of the Graphite||PBA full cell in 1 M TMP electrolyte.

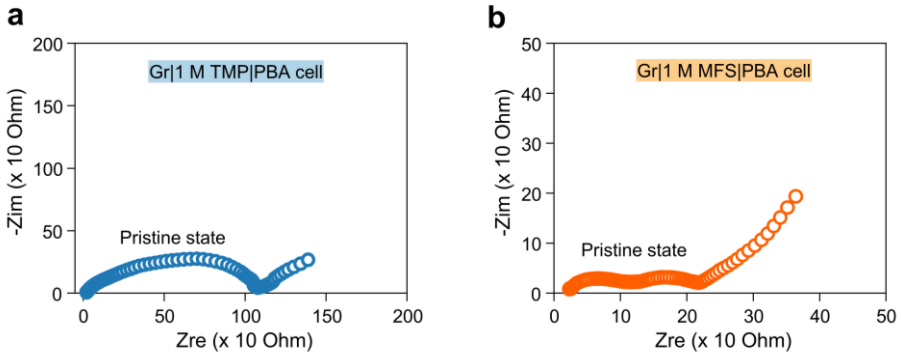

Supplementary Fig. 79. **a**, **b**, The EIS of the Graphite||PBA full cell in the pristine state with 1 M TMP (**a**) and 1 M MFS (**b**) electrolytes.

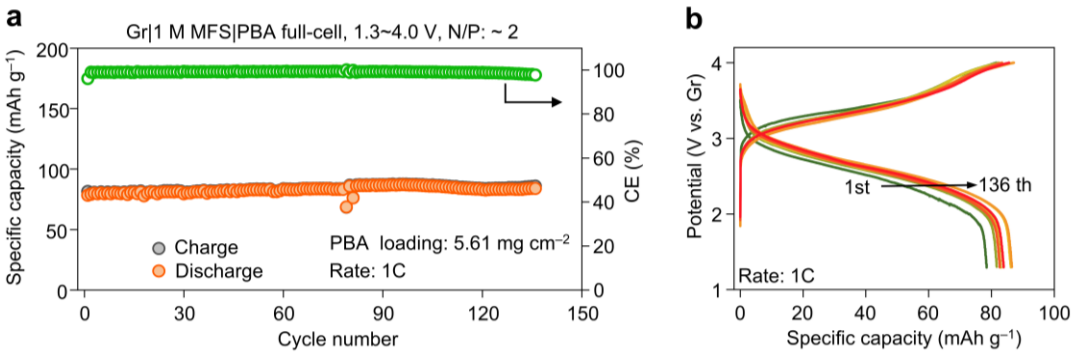

Supplementary Fig. 80. **a**, **b**, Cycling performance (**a**) and corresponding charge–discharge curves (**b**) of Graphite||PBA full cell with a high PBA positive electrode loading of 5.61 mg cm^{-2}.

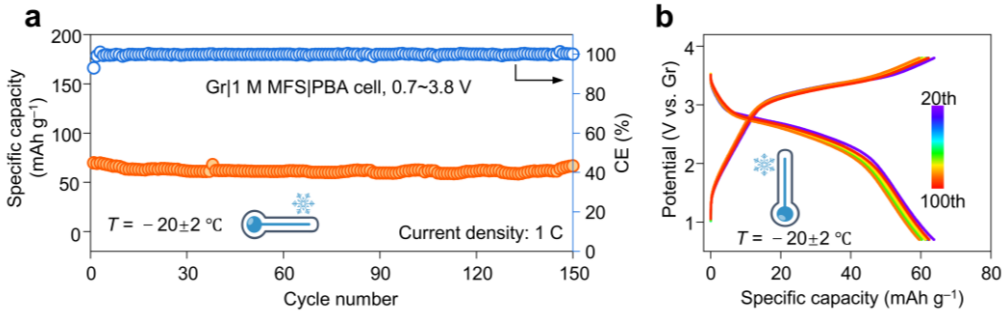

Supplementary Fig. 81. **a**, **b**, Cyclic stability (**a**) and corresponding charge–discharge curves (**b**) of the Graphite||PBA full cell in 1 M MFS electrolyte at –20 ± 2 °C.

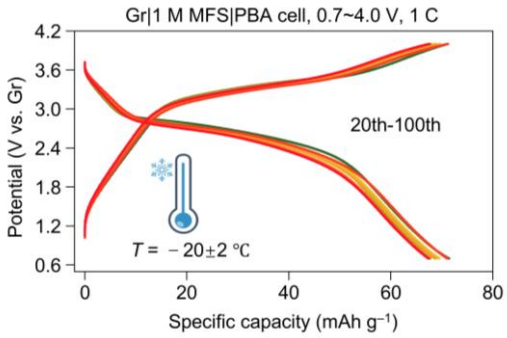

Supplementary Fig. 82. Charge-discharge curves of the Graphite||PBA full cell with 1 M MFS electrolyte at –20 ± 2 °C.

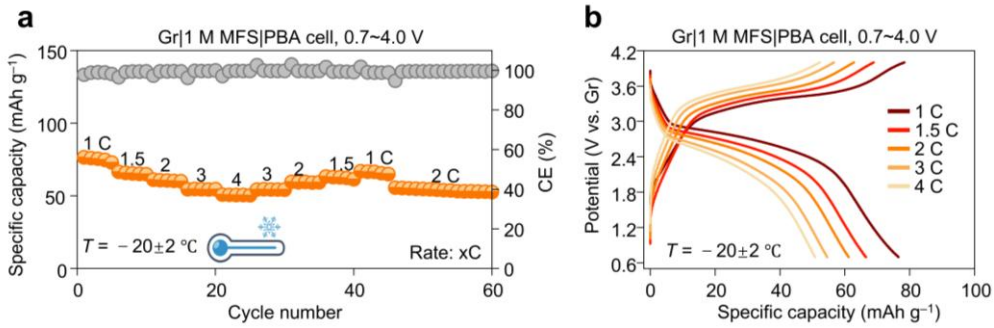

Supplementary Fig. 83. **a**, **b**, Rate performance (**a**) and corresponding charge-discharge curves (**b**) of the Graphite||PBA full cell in 1 M MFS electrolyte at –20 ± 2 °C.

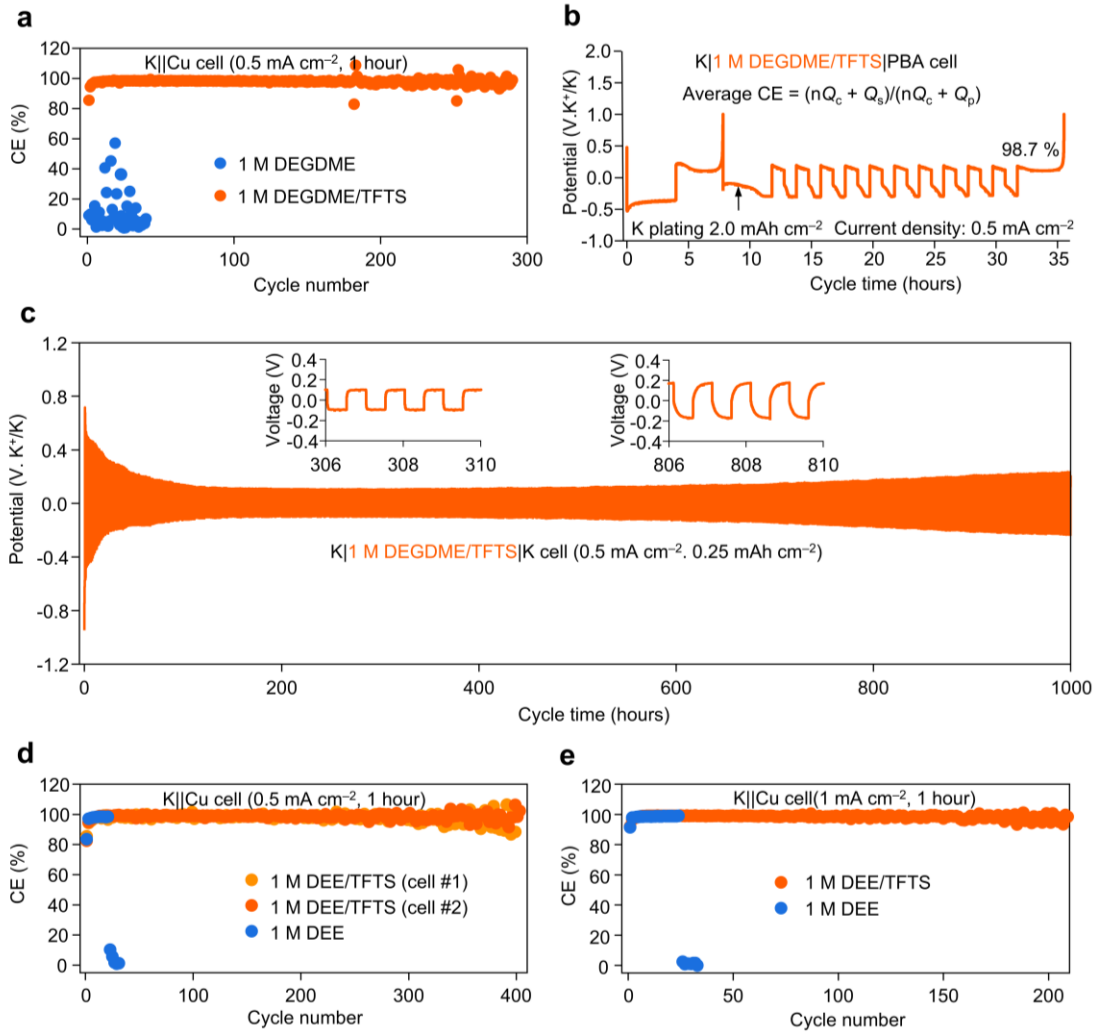

Supplementary Fig. 84 | Verification of the universality of the TFTS-mediated strategy in ether-based electrolytes. a, **b**, CE of K plating-stripping in K||Cu cells

with 1 M DEGDME electrolyte and 1 M DEGDME/TFTS electrolyte. **c**, Long-cycle performance of K||K cells with 1 M DEGDME/TFTS electrolyte. **d**, **e**, CE and cycling stability of K||Cu cells using 1 M DEE electrolyte and 1 M DEE/TFTS electrolyte. Tetraethylene glycol dimethyl ether: DEGDME; Ethylene glycol diethyl ether: DEE.

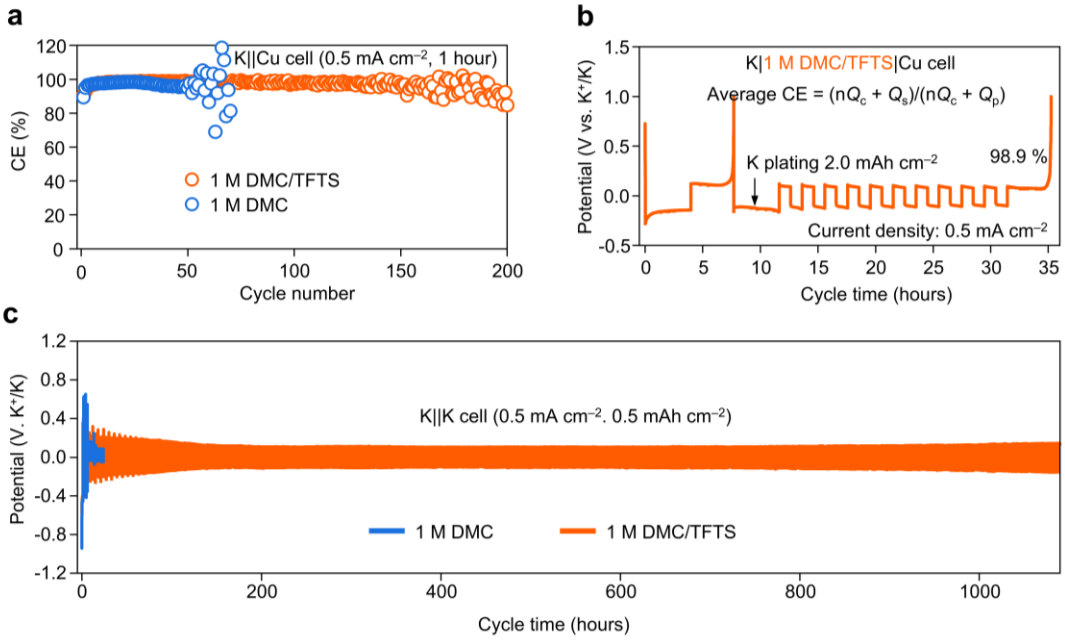

Supplementary Fig. 85 | Verification of the universality of the TFTS-mediated strategy in dimethyl carbonate (DMC)-based electrolyte using K||Cu and K||K cells. a, **b**, CE of K plating-stripping in K||Cu cells with 1 M DMC electrolyte and 1 M DMC/TFTS electrolyte. **c**, Long-cycle performance of K||K cells with 1 M DMC and 1 M DMC/TFTS electrolytes.

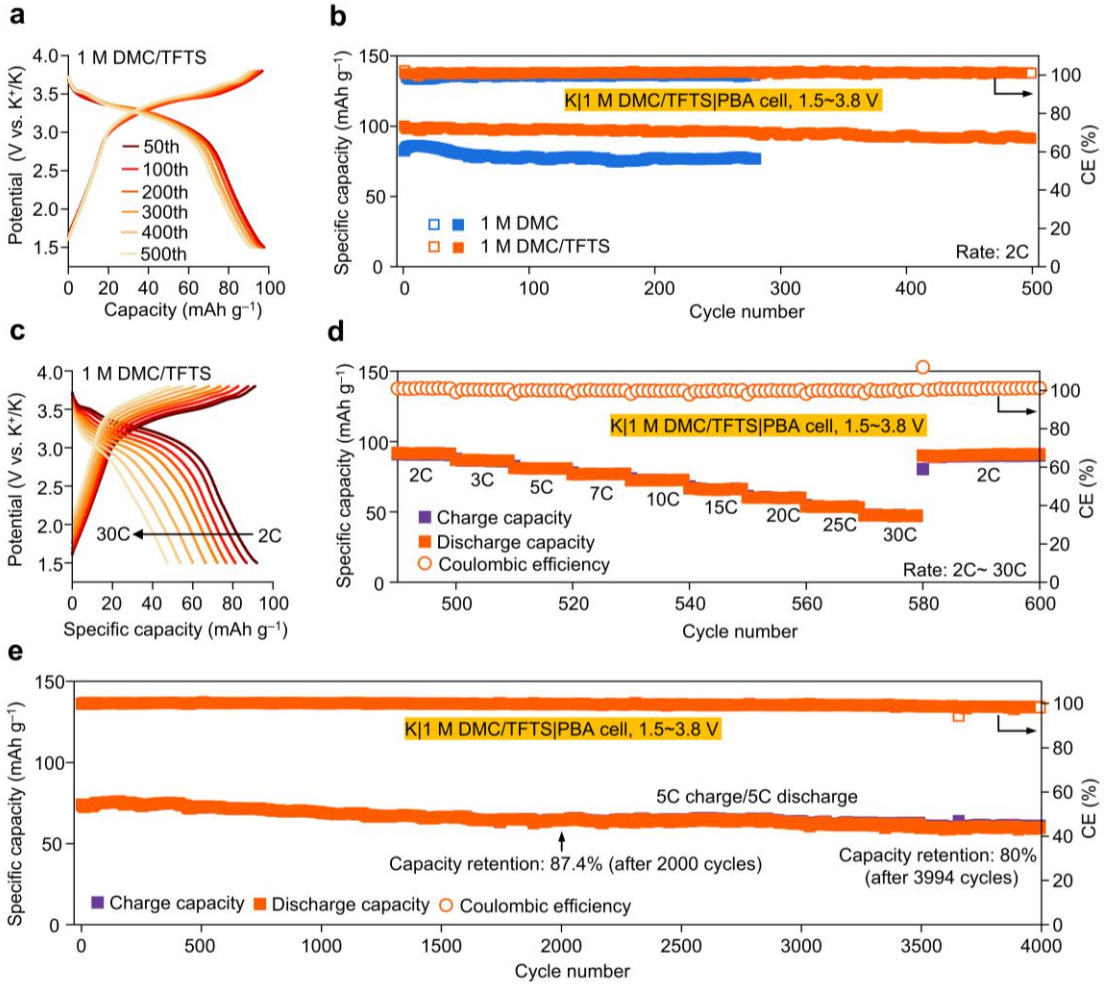

Supplementary Fig. 86 | Verification of the universality of the TFTS-mediated strategy in DMC-based electrolyte using K||PBA cells. a, Charge-discharge voltage profiles of the K||PBA cell in 1 M DMC/TFTS electrolyte. **b**, Cycling stability of the K||PBA cell using 1 M DMC electrolyte and 1 M DMC/TFTS electrolyte. **c**, **d** Rate performance and corresponding charging-discharging voltage profiles of K||PBA cell in 1 M DMC/TFTS electrolyte, performed after 500 cycling tests at 2 C in (**b**). **e**, Long cycling stability of the K||PBA cell at 5 C in 1 M DMC/TFTS electrolyte.

Supplementary Note 1: As show in Supplementary Fig. 30, due to the unique K^+ solvation structure that is induced TFTS solvent, the ionic conductivity of 1M MFS electrolyte (1.74 mS cm^{-1}) is only slightly lower than that of the 1 M TMP electrolyte (2.49 mS cm^{-1}). However, for the traditional, and classic LHCE (1 M TMP/TTE, 0.97 mS cm^{-1}), which suffers a significant conductivity loss due to the tight cation-anion aggregation and the no-solvating ability of TTE. This result indicates that the overall bulk conductivity of 1 M MFS electrolyte is largely maintained, in stark contrast to the traditional 1 M TMP/TTE electrolyte. More importantly, the 1M MFS electrolyte exhibits the highest K^+ transference number (0.54) among the three electrolytes (Supplementary Fig. 27 and Supplementary Fig. 31), which compensates for its slightly reduced conductivity and ensures rapid K^+ transport kinetics for efficient battery operation. This combination is the definitive evidence for our claimed decoupling of bulk ion transport and interfacial chemistry. Unlike the traditional 1 M TMP/TTE electrolyte, which improves interfacial stability at the expense of bulk conductivity, our 1 M MFS electrolyte achieves a remarkable interface stability while preserving competent high ion transport kinetics, facilitated by a unique K^+ solvation structure. Overall, this precisely demonstrates that the bulk transportation and interfacial chemistry have been successfully decoupled and independently optimized through our unique solvation structure engineering.

Table S1. HOMO of solvent molecules in a vacuum environment.

Solvents	HOMO (eV)	LUMO (eV)
Ethylene carbonate (EC)	− 8.454	− 0.535
Diethyl carbonate (DEC)	− 8.012	− 0.169
Dimethyl carbonate (DMC)	− 8.176	− 0.159
Trimethyl phosphate (TMP)	− 8.113	− 0.195
Ethyl mesylate (EM)	− 8.208	− 0.396
2,2,2-trifluoroethyl trifluoromethanesufonate (TFTS)	− 9.914	− 0.931

Table S2. Fitted interfacial resistance ($R_{interfacial}$) values form EIS of K||K cells in the 1 M TMP electrolyte (Supplementary Fig. 26b).

T (K)	1000/T (K^{-1})	$R_{interfacial}$ (Ohm)	ln(1/$R_{interfcial}$)
293	3.41	14428	− 9.58
298	3.35	7600	− 8.94
303	3.30	4443	− 8.40
308	3.24	2709	− 7.90
313	3.19	1729	− 7.45
318	3.14	1152	− 7.05
323	3.09	787	− 6.67

Table S3. Fitted interfacial resistance ($R_{interfacial}$) values form EIS of K||K cells in the 1 M MFS electrolyte (Supplementary Fig. 26a).

T (K)	1000/T (K^{-1})	$R_{interfacial}$ (Ohm)	ln(1/$R_{interfcial}$)
293	3.41	2838	− 7.95
298	3.35	1784	− 7.49
303	3.30	1028	− 6.93
308	3.24	686	− 6.53
313	3.19	464	− 6.14
318	3.14	303	− 5.71
323	3.09	162	− 5.09

Table S4. Fitted interfacial resistance ($R_{interfacial}$) values form EIS of K||K cells in the1 M TMP/TTE electrolyte (Supplementary Fig. 32a).

T (K)	1000/T (K^{-1})	$R_{interfacial}$ (Ohm)	ln(1/$R_{interfcial}$)
293	3.41	12301	− 9.42
298	3.35	7090	− 8.87
303	3.30	3056	− 8.02
308	3.24	1626	− 7.39
313	3.19	822	− 6.71
318	3.14	343	− 5.83
323	3.09	282	− 5.64

Table S5. Fitted interfacial resistance ($R_{interfacial}$) values form EIS of K|K@C ref.|PBA cell cells in 1 M TMP electrolyte (Supplementary Fig. 55).

T (K)	1000/T (K^{-1})	$R_{interfacial}$ (Ohm)	ln(1/$R_{interfcial}$)
293	3.41	620	− 6.43
298	3.35	361	− 5.89
303	3.30	221	− 5.40
308	3.24	135	− 4.91
313	3.19	85	− 4.44
318	3.14	55	− 4.01
323	3.09	38	− 3.64

Table S6. Fitted interfacial resistance ($R_{interfacial}$) values form EIS of K|K@C ref.|PBA cells in the 1 M MFS electrolyte (Supplementary Fig. 56a).

T (K)	1000/T (K^{-1})	$R_{interfacial}$ (Ohm)	ln(1/$R_{interfcial}$)
293	3.41	268	− 5.59
298	3.35	206	− 5.33
303	3.30	160	− 5.07
308	3.24	122	− 4.80
313	3.19	92	− 4.52
318	3.14	61	− 4.11
323	3.09	31	− 3.42

Table S7. Fitted interfacial resistance ($R_{interfacial}$) values form EIS of K|K@C ref.|PBA cells in the 1 M KFSI TMP/TTE electrolyte (Fig. 4d).

T (K)	1000/T (K^{-1})	$R_{interfacial}$ (Ohm)	ln(1/$R_{interfcial}$)
293	3.41	475	− 6.16
298	3.35	219	− 5.39
303	3.30	178	− 5.18
308	3.24	114	− 4.74
313	3.19	80	− 4.38
318	3.14	60	− 4.09
323	3.09	40	− 3.70

Table S8. Fitted SEI film resistance (R_f) and charge-transfer resistance (R_{ct}) values from EIS of K||K cells after 5 cycles (Figure 5e).

Electrolytes	R_f	R_{ct}	Total error (%)
1 M TMP	83	555	1.64%
1 M MFS	70	261	2.09%

Supplementary References

1. Wahyudi W, et al. Hitherto unknown solvent and anion pairs in solvation structures reveal new insights into high-performance lithium-ion batteries. *Adv. Sci.* **9**, 2202405 (2022).

2. Tian Y-F, et al. Insights into anion–solvent interactions to boost stable operation of ether-based electrolytes in pure-SiO_x||$LiNi_{0.8}Mn_{0.1}Co_{0.1}O_2$ full cells. *Angew. Chem. Int. Ed.* **62**, e202305988 (2023).

3. Zhou X, Zhang Q, Zhu Z, Cai Y, Li H, Li F. Anion-reinforced solvation for a gradient inorganic-Rich interphase enables high-rate and stable sodium batteries. *Angew. Chem. Int. Ed.* **61**, e202205045 (2022).

4. Jang J, et al. Miniature Li^+ solvation by symmetric molecular design for practical and safe Li-metal batteries. *Nat. Energy* **10**, 502-512 (2025).